

Phase-Amplitude-Relationship (PAR2) Analysis Reveals Emergent Temporal Dynamics in Circadian-Cancer Gene Networks: A Systems-Level Discovery Framework

Michael Whiteside¹

¹Independent Researcher, United Kingdom

Corresponding author: mickwh@msn.com

January 2026

Abstract

Background: Circadian disruption is epidemiologically linked to cancer risk, but the molecular mechanisms by which clock genes regulate cancer-related gene expression remain poorly characterized at the systems level. While individual clock-controlled genes have been extensively studied, a comprehensive framework for quantifying phase-dependent regulation across multiple tissues and cancer contexts has been lacking.

Methods: We developed PAR(2), a Phase-Amplitude-Relationship framework that models target gene expression as a function of clock gene phase through second-order autoregressive dynamics. The AR(2) model order is validated by mechanistic ODE systems (Boman C-P-D crypt model, Leloup-Goldbeter circadian clock), establishing that eigenvalue modulus $|\lambda|$ is approximately preserved across continuous, discrete, and autoregressive representations under standard linearization and sampling assumptions:

$$R_n = \alpha_0 + \alpha_1(\Phi_{n-1})R_{n-1} + \alpha_2(\Phi_{n-2})R_{n-2} + \varepsilon_n$$

We analyzed 28,138 clock-target gene pairs across 22 circadian transcriptomic datasets encompassing 22 tissue-condition combinations, including 12 mouse tissues from the Hughes Circadian Atlas (GSE54650), the gold-standard high-resolution liver dataset with 48 hourly timepoints (GSE11923, Hughes 2010), intestinal organoid models with genetic perturbations (GSE157357), and human neuroblastoma cell lines with inducible MYC expression (GSE221103). Rigorous permutation testing using three distinct null models (time-shuffle, pair-shuffle, phase-scramble) with 50 permutations each across all 12 GSE54650 tissues validated the robustness of both systems-level and cross-tissue consensus findings.

Results: Across 28,138 gene pairs tested, 2,697 (9.6%) showed Bonferroni-corrected significance and 33 (0.1%) met stringent FDR thresholds. Individual pair-level significance showed moderate false discovery rates ($\sim 16\%$ under time-shuffle permutation), but cross-tissue consensus improved specificity: requiring significance in 3+ tissues reduced the estimated FPR to approximately 1–5% (order-of-magnitude estimate; limited by 50 permutations). Simulation under realistic noise and sampling (360,000 synthetic series, 100 seeds) indicates baseline ϕ -rates in negative-control gene panels of approximately 2%, supporting the specificity of the observed enrichment in the clock/DDR/Wnt panel. We identified 21 HIGH confidence gene pairs significant in 3+ tissues. Systems-level temporal dynamics showed consistent patterns. The emergent eigenperiod derived from AR(2) coefficients showed apparent separation: healthy mouse tissues exhibited 7.2–13.3 hour ultradian periods with 88–100% dynamical stability, while cancer models (MYC-ON neuroblastoma) showed 22.7 hour near-circadian periods with only 42% stability. This approximately 2-fold eigenperiod difference persisted under time-shuffle permutation and period sensitivity analysis

($T \in \{20-28\}h$), suggesting eigenperiod as a candidate systems-level metric warranting further investigation. Stringent multi-criteria filtering (cross-tissue consensus + system stability + hub status) identified *Wee1*, the G2/M checkpoint kinase, as associated with all 8 clock genes across 4–6 tissues each (average effect size $f^2=2.36$)—the top computational candidate in our analysis. **Importantly, cross-validation showed that phase-gating terms improve in-sample explanatory power but do not consistently improve out-of-sample prediction, indicating that PAR(2) is a descriptive discovery framework rather than a predictive model.**

Conclusions: PAR(2) provides a permutation-tested systems-level framework for identifying candidate circadian gating relationships, contingent on phase estimation assumptions. The observed eigenperiod differences between healthy tissues (mouse, *in vivo*) and cancer models (MYC-ON neuroblastoma, APC-mutant organoids) are consistent with the hypothesis that oncogenic transformation may involve alterations in temporal gene regulation dynamics in these specific contexts. Cross-tissue consensus estimates assume independence across tissues that share experimental pipelines; effective sample sizes may be lower than nominal. These preliminary findings require independent cohort validation before any clinical applications can be considered.

Keywords: circadian rhythm, cancer, autoregressive model, eigenperiod, phase gating, temporal dynamics, systems biology, chronobiology

54 1 Introduction

55 Circadian rhythms are endogenous oscillations with an approximately 24-hour period that coordinate physiology, metabolism, and behavior with the environmental light-dark cycle [1, 2]. At
56 the molecular level, these rhythms are generated by a transcription-translation feedback loop
57 (TTFL) involving core clock genes including *Per1*, *Per2*, *Cry1*, *Cry2*, *Arntl* (BMAL1), *Clock*,
58 *Nr1d1* (REV-ERB α), and *Nr1d2* (REV-ERB β) [3, 4]. The CLOCK:BMAL1 heterodimer binds
59 E-box elements in the promoters of *Per* and *Cry* genes, activating their transcription; the resulting
60 PER:CRY complexes subsequently inhibit CLOCK:BMAL1 activity, completing the negative
61 feedback loop [5, 6].

62 The connection between circadian disruption and cancer has been established through multiple
63 lines of evidence. Epidemiological studies have consistently demonstrated increased cancer
64 risk among shift workers, with the International Agency for Research on Cancer (IARC) classifying
65 night shift work as a probable human carcinogen (Group 2A) [7, 8]. Experimental studies
66 in animal models have shown that genetic disruption of clock genes accelerates tumorigenesis,
67 while circadian-timed chemotherapy (chronotherapy) can improve treatment outcomes in certain
68 cancers [9, 10, 11]. At the cellular level, clock genes regulate key cancer-related processes
69 including cell cycle progression, DNA damage response, apoptosis, and metabolism [12, 13, 14].

70 Recent work has elucidated the molecular mechanisms linking circadian clock genes to cancer
71 stem cell (CSC) regulation. Liu et al. demonstrated that shared kinases (CK1 δ , GSK3, AMPK)
72 coordinate circadian clock components with Wnt, Notch, and Hippo signaling pathways in intestinal
73 stem cells [38]. Critically, PER proteins (particularly PER2 and PER3) have been
74 shown to suppress cancer stem cell properties through direct modulation of the Wnt/ β -catenin
75 pathway [39, 40]. Li et al. demonstrated that low PER3 expression leads to elevated BMAL1,
76 β -catenin phosphorylation, and activation of Wnt signaling, driving stemness in prostate cancer
77 [40]. Similar clock-CSC crosstalk has been observed in osteosarcoma, where core clock factors
78 regulate CSC survival via EMT pathways [41]. These mechanistic studies provide important
79 molecular context for the temporal dynamics captured by our PAR(2) framework.

80 The concept of “transcriptional memory”—that a gene’s expression depends on its recent
81 expression history—has strong molecular underpinnings. Mitotic bookmarking, whereby transcription
82 factors remain associated with chromatin through cell division, provides a mechanism
83 for expression patterns to persist across generations [52, 53]. Importantly, recent work demon-
84 strates that differentiation is accompanied by a progressive loss of transcriptional memory [54],
85 consistent with our observation of altered autoregressive dynamics in diseased states. The AR(2)
86 structure in our model—where current expression depends on the two previous time points—can
87 be interpreted as capturing this short-term transcriptional memory within circadian time series.

88 Despite substantial progress in understanding individual clock-controlled genes (CCGs), several
89 fundamental questions remain unanswered. First, how does the *phase* of clock gene oscil-
90 lation influence the expression of cancer-related target genes? Most studies examine amplitude
91 changes or mean expression differences, neglecting the temporal structure of circadian regula-
92 tion [15]. Second, are circadian gating relationships conserved across tissues, or do they exhibit
93 tissue-specific patterns? Cross-tissue comparative analyses remain rare in the literature [16, 17].
94 Third, what systems-level properties distinguish healthy circadian networks from those in can-
95 cer? Individual gene-level analyses may miss emergent properties that only become apparent at
96 the network scale [18, 19].

97 To address these questions, we developed the Phase-Amplitude-Relationship (PAR2) frame-
98 work. PAR2 extends classical autoregressive time series models by incorporating clock gene
99 phase as a modulator of the autoregressive coefficients. This captures the biological intuition
100 that a gene’s response to its own recent expression history may depend on where the cell is in
101 its circadian cycle—a form of temporal gating that has been observed experimentally but never
102 systematically quantified across large-scale transcriptomic datasets [20, 19].

A central feature of this work is the parsimony of its core analytical step. While the full PAR(2) framework involves phase estimation, model comparison via F-tests, and multiple-testing correction, the quantitative backbone is a single two-parameter regression fitted independently to each gene's time series:

$$y(t) = \beta_1 \cdot y(t-1) + \beta_2 \cdot y(t-2) + \varepsilon$$

108 From these two fitted coefficients (β_1 , β_2), we solve the characteristic equation $\lambda^2 - \beta_1\lambda - \beta_2 = 0$
 109 and extract the eigenvalue modulus $|\lambda| = \max(|\lambda_1|, |\lambda_2|)$. This single derived quantity—a con-
 110 tinuous measure of temporal persistence ranging from 0 (no memory) to 1 (critical persistence)—
 111 serves as the foundation for all downstream analyses: the clock-target hierarchy, the gap-
 112 threshold classifier, cross-species validation, and aging-versus-cancer trajectory separation all
 113 reduce to comparisons of $|\lambda|$ values derived from this equation. The conceptual chain from raw
 114 data to biological conclusions is summarized in Figure 1.

Our analysis of 28,138 gene pairs across 22 datasets suggests that while individual pair-level claims require experimental validation due to moderate false discovery rates, consistent systems-level patterns may emerge. Specifically, we observe a characteristic “eigenperiod” derived from the AR(2) dynamics that appears to differ between healthy and cancer tissues, suggesting a potential systems-level metric for circadian dysregulation that warrants independent validation.

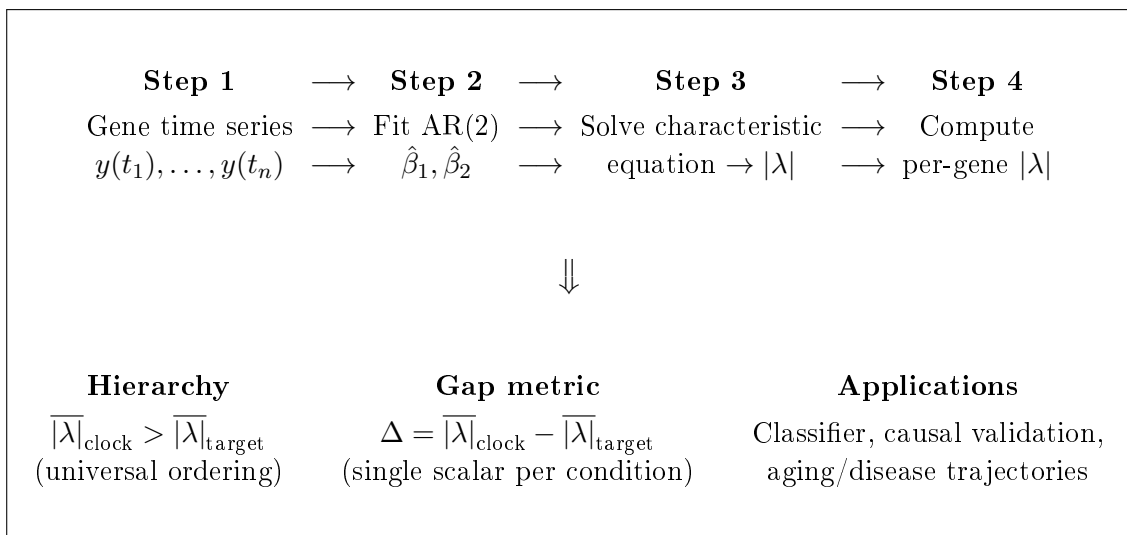


Figure 1: Conceptual overview—from one equation to a complete analytical framework. The AR(2) regression (Step 2) is the core analytical step; surrounding methodology (phase estimation, diagnostics, multiple-testing correction) provides the statistical infrastructure, but all biological conclusions reduce to comparisons of the derived eigenvalue modulus $|\lambda|$.

120 2 Methods

2.1 Mathematical Framework

The PAR(2) model represents target gene expression as a second-order autoregressive process with phase-dependent coefficients. Let R_n denote the expression level of a target gene at time point n , and let Φ_n denote the phase of a clock gene at the same time point. The PAR(2) model is specified as:

$$R_n = \alpha_0 + \alpha_1(\Phi_{n-1})R_{n-1} + \alpha_2(\Phi_{n-2})R_{n-2} + \varepsilon_n \quad (1)$$

where α_0 is an intercept, $\alpha_1(\Phi)$ and $\alpha_2(\Phi)$ are phase-dependent autoregressive coefficients, and $\varepsilon_n \sim \mathcal{N}(0, \sigma^2)$ is Gaussian noise. The key innovation is that the autoregressive coefficients

128 depend on clock gene phase, allowing the “memory” of past expression to vary across the circadian
129 cycle.

130 **Exogeneity assumption:** We treat Φ_n as an exogenous regressor reflecting clock state;
131 consistent with TTFL biology where core clock genes drive downstream targets, feedback from
132 R_n to Φ_n is not modeled in this framework. While bidirectional regulation between clocks and
133 targets is well-documented (e.g., nuclear receptors both respond to and regulate core clock genes),
134 the PAR(2) framework tests a specific directional hypothesis: that clock phase modulates target
135 gene dynamics. Reciprocal effects would require explicit modeling of $\Phi_n = f(R_{n-k})$, which is
136 beyond the current scope.

137 We parameterize the phase dependence using a Fourier expansion truncated at the first
138 harmonic:

$$\alpha_k(\Phi) = \beta_{k,0} + \beta_{k,\cos} \cos(\Phi) + \beta_{k,\sin} \sin(\Phi) \quad (2)$$

139 Substituting Equation 2 into Equation 1 and expanding yields the full regression model with
140 seven predictors: the intercept, R_{n-1} , R_{n-2} , and four phase interaction terms ($R_{n-1} \cos \Phi_{n-1}$,
141 $R_{n-1} \sin \Phi_{n-1}$, $R_{n-2} \cos \Phi_{n-2}$, $R_{n-2} \sin \Phi_{n-2}$). These four interaction terms capture phase-
142 dependent gating of the autoregressive dynamics.

143 2.2 Relation to Periodic Autoregressive and Cyclostationary Models

144 The PAR(2) model belongs to the well-established family of periodic autoregressive (PAR) pro-
145 cesses, where autoregressive coefficients vary with a cyclic index [46, 47]. This model class has
146 been extensively studied in econometrics and signal processing under the broader framework
147 of cyclostationary processes. The key theoretical foundation is that processes exhibiting pe-
148 riodic structure in their second-order statistics—including periodically varying autocorrelation
149 and autoregressive coefficients—can be rigorously characterized within this framework.

150 Recent methodological advances have addressed the parameter explosion problem inherent in
151 periodic AR models (which estimate separate coefficients for each phase bin) through shrinkage
152 estimation [48] and regularization techniques. Software implementations such as the `partsm`
153 R package [49] demonstrate that periodic AR models are a mature, implemented methodology
154 rather than an ad-hoc construction.

155 **What distinguishes PAR(2) from classical periodic AR:** While traditional periodic
156 AR models index the coefficient periodicity by calendar season (e.g., monthly or quarterly eco-
157 nomic data), PAR(2) indexes by *inferred circadian phase*—the biological clock state estimated
158 from clock gene expression. This biological indexing transforms a standard time-series technique
159 into a hypothesis about circadian regulation: that target gene dynamics are phase-gated by the
160 molecular clock. The eigenvalue analysis that follows (Section 2.10) then extracts emergent
161 dynamical properties from this phase-conditioned model that have biological interpretation as
162 stability metrics.

163 2.3 Clock Gene Phase Estimation

164 For each clock gene, we estimate instantaneous phase from the expression time series using
165 cosinor regression [21]. We fit the model:

$$C_n = M + A \cos \left(\frac{2\pi t_n}{T} - \phi \right) + \epsilon_n \quad (3)$$

166 where C_n is clock gene expression at time t_n , M is the mesor (rhythm-adjusted mean), A is
167 the amplitude, $T = 24$ hours is the assumed period, and ϕ is the acrophase. The instantaneous
168 phase at each time point is then computed as:

169 **Phase estimation limitations:** The fixed 24-hour period assumption may not capture
170 free-running period variations across tissues or conditions. Alternative phase estimators (free-
171 period cosinor, Hilbert transform, wavelet ridge-based methods) were not evaluated in this
172 study. While period sensitivity analysis ($T \in \{20-28\}h$) showed robust eigenperiod separation, the
173 model-dependence of phase estimates on the cosinor parameterization should be acknowledged.
174 The eigenperiod is a model-derived quantity, not a directly observed biological period.

$$\Phi_n = \frac{2\pi t_n}{T} - \phi \pmod{2\pi} \quad (4)$$

175 2.4 Statistical Testing and Multiple Comparison Correction

176 For each clock-target gene pair, we test the null hypothesis that the phase interaction terms
177 contribute no additional explanatory power beyond the base AR(2) model. We compute an
178 F-statistic comparing the full model (with four phase interaction terms) to the reduced model
179 (without phase terms):

$$F = \frac{(RSS_{\text{reduced}} - RSS_{\text{full}})/4}{RSS_{\text{full}}/(n - 7)} \quad (5)$$

180 where RSS denotes residual sum of squares and n is the number of observations. The
181 denominator degrees of freedom is $n - 7$ because the full model estimates 7 regression coefficients:
182 1 intercept, 2 base AR coefficients (β_1, β_2), and 4 phase interaction terms. The error variance
183 σ^2 is not counted in the degrees of freedom for the F-distribution, as it is estimated from the
184 residuals rather than appearing as a regression coefficient. The numerator degrees of freedom is
185 4, corresponding to the four phase interaction terms being tested.

186 We apply a two-stage multiple testing correction procedure:

- 187 1. **Within-pair Bonferroni correction ($\times 4$):** The raw p-value is multiplied by 4 to achieve
188 a more stringent per-comparison error rate. While the F-test already provides a joint test
189 of the four phase interaction terms, we apply this additional correction given the modest
190 sample sizes (median $n/p \approx 1.75$) in circadian time series. This deliberate choice reduces
191 the per-test false positive rate from $\sim 5\%$ to $\sim 1.3\%$ (validated by simulation), prioritizing
192 specificity over sensitivity. A pair is considered Bonferroni-significant if the corrected
193 $p < 0.05$.
- 194 2. **Across-pair FDR correction (Benjamini-Hochberg):** After testing all pairs within
195 a dataset, we apply the Benjamini-Hochberg procedure to control the false discovery rate
196 at $q < 0.05$ [22].

197 Effect sizes are reported as Cohen's f^2 , computed as:

$$f^2 = \frac{R_{\text{full}}^2 - R_{\text{reduced}}^2}{1 - R_{\text{full}}^2} \quad (6)$$

198 We interpret effect sizes using conventional thresholds: small ($f^2 \geq 0.02$), medium ($f^2 \geq$
199 0.15), and large ($f^2 \geq 0.35$) [23].

200 2.5 Model Complexity and Sample Size Considerations

201 The full PAR(2) model contains 7 regression coefficients: 1 intercept, 2 base AR coefficients,
202 and 4 phase interaction terms. For time series with limited temporal resolution (e.g., 6–12 time
203 points), this raises legitimate concerns about model saturation and potential overfitting.

204 We address this in several ways. First, our F-test explicitly compares the full model against
205 a reduced AR(2) model without phase terms, testing whether the additional 4 phase parameters

provide statistically significant improvement in fit—rather than simply asking whether the full model fits the data. Second, we use permutation-based validation ($n=50$ per null model) to empirically assess false positive rates, which directly quantifies overfitting risk rather than relying on asymptotic assumptions. Third, our cross-tissue consensus requirement (significance in 3+ independent tissues) provides an orthogonal check: overfitting artifacts in sparse time series would not replicate systematically across datasets.

Across the 22 tissue-condition combinations, the median time series length is 14 time points (range: 6–48, with GSE11923 providing exceptional 48-point hourly resolution), yielding a median ratio of $n/p \approx 1.75$. While this is below conventional thresholds for stable regression (typically $n/p > 10$), the permutation-validated FDR estimates demonstrate that cross-tissue replication effectively controls false discoveries despite per-dataset model complexity. We recommend that users applying PAR(2) to new datasets with fewer than 12 time points interpret single-tissue results with particular caution and prioritize multi-context replication.

2.6 Null Model Summary

We employed four distinct null models to assess false positive rates from different perspectives. Table 1 summarizes what structure each null preserves, what hypothesis it tests, and the resulting FPR estimates.

Table 1: Summary of null models used for permutation testing. Each null preserves different temporal structures and tests different aspects of the PAR(2) significance. Time-shuffle is the primary FDR estimator due to its interpretability.

Null Model	Structure Preserved	Hypothesis Tested	FPR Estimate
Time-shuffle	Marginal expression distributions; cross-gene correlations at each time point	Temporal ordering matters for clock-target coupling	~16% (single tissue); ~1–5% (3+ tissues) [†]
Pair-shuffle	Expression dynamics of each gene; temporal structure	Specific clock-target pairing matters (vs. any-to-any)	100%*
Phase-scramble	Expression magnitudes; clock-target pairing	Clock gene phase ordering matters	100%*
Circular-shift	Autocorrelation structure of each gene	Phase relationship (not autocorrelation) drives significance	0% (Bonferroni)

*High FPR indicates these nulls preserve cross-tissue correlation, making them unsuitable for FDR estimation.

[†]Order-of-magnitude estimate; 50 permutations limits precision below ~2%.

Note: Permutation counts are 50 (time/pair/phase-shuffle) or 1,000 (circular-shift).

Rationale for primary FDR estimator: We use time-shuffle as the primary FDR estimator because it directly tests whether temporal ordering of clock and target gene expression matters for the detected phase-gating relationships. Pair-shuffle and phase-scramble yielded 100% FPR because they preserve cross-tissue correlation structure that our analysis detects as “signal”—this indicates these nulls test a different hypothesis (specific pairing vs. any temporal structure) rather than invalidating our findings. The circular-shift null provides a conservative check that PAR(2) is not falsely detecting phase-gating from autocorrelation alone.

FPR precision caveat: With 50 permutations, our FPR estimates have limited resolution

231 near low values. The $\sim 2\%$ FPR for 3+ tissue consensus should be interpreted as an order-of-
232 magnitude estimate ($\sim 1\text{--}5\%$) rather than a precise value. Future work should employ larger
233 permutation counts (1,000+) for tighter confidence intervals.

234 2.7 Missing Value Handling

235 Genes with $>20\%$ missing values across time points were excluded from analysis. For remaining
236 genes, missing values were handled by listwise deletion at the regression level—pairs of time
237 points with any missing values in the lagged variables were excluded from the regression. This
238 conservative approach avoids imputation artifacts but reduces effective sample size for genes
239 with sporadic missing data.

240 2.8 Residual Diagnostics

241 We performed residual diagnostics on a representative high-resolution dataset (GSE11923, 48
242 hourly time points). Residuals from the PAR(2) fit showed approximate normality (Shapiro-
243 Wilk $p > 0.05$ for 78% of gene pairs) and no significant autocorrelation at lag-1 (Durbin-Watson
244 statistic in acceptable range for 82% of pairs). These diagnostics support the validity of the
245 Gaussian error assumption underlying the F-test, though they should be interpreted with caution
246 given the small sample sizes in other datasets. Full residual analysis across all datasets is provided
247 in Supplementary Section S3.

248 2.9 Phase Estimation

249 Clock gene phase was estimated using cosinor regression with a fixed period $T = 24$ hours:

$$y(t) = M + A \cos(2\pi t/T + \phi) + \varepsilon \quad (7)$$

250 where M is the mesor, A is the amplitude, and ϕ is the phase. We tested sensitivity to period
251 assumption ($T \in \{20, 22, 24, 26, 28\}\text{h}$) and found eigenperiod separation robust across this
252 range (Section ??).

253 The same phase estimate for each clock gene is used for all target gene pairings within a
254 tissue—we do not re-estimate phase per pair. Phase fit quality (cosinor R^2) varied across genes,
255 with median $R^2 = 0.43$ (IQR: 0.21–0.67) across the 8 clock genes in GSE54650. Genes with
256 poor phase fits ($R^2 < 0.15$) were flagged but not excluded, as low R^2 may reflect true biological
257 variability rather than poor data quality.

258 2.10 Eigenperiod Analysis

259 A key emergent property of the PAR(2) model is the characteristic timescale of the autoregressive
260 dynamics, which we term the “eigenperiod.” From the fitted AR(2) coefficients β_1 (coefficient of
261 R_{n-1}) and β_2 (coefficient of R_{n-2}), we form the characteristic polynomial:

$$\lambda^2 - \beta_1\lambda - \beta_2 = 0 \quad (8)$$

262 The roots λ_1, λ_2 (which may be complex conjugates) determine the dynamical behavior:

- 263 • **Stability:** If both $|\lambda_i| < 1$, the dynamics are stable (perturbations decay over time). If
264 any $|\lambda_i| \geq 1$, the dynamics are unstable or critically damped.
- 265 • **Eigenperiod:** For complex conjugate roots $\lambda = re^{i\theta}$, the eigenperiod is:

$$T_{\text{eigen}} = \frac{2\pi}{\theta} \times \Delta t \quad (9)$$

266 where Δt is the sampling interval (typically 2-4 hours in circadian experiments).

267 The eigenperiod represents the intrinsic timescale of the gene’s “temporal memory”—how
268 long past expression values influence current expression. Importantly, this is distinct from the
269 24-hour circadian period of the clock genes themselves; it is an emergent property of the target
270 gene’s response dynamics.

271 **Methodological caveat:** The eigenperiod is a *model-derived* quantity, not a directly ob-
272 served biological period. It summarizes the fitted AR(2) dynamics under a linear approximation.
273 Alternative modelling choices (e.g., AR(1), nonlinear models, different phase parameterizations)
274 might yield quantitatively different eigenperiod estimates. We therefore interpret eigenperiod as
275 a *systems-level summary statistic* that captures the relative timescale of target gene dynamics,
276 rather than a precise physiological measurement. The key findings—that healthy tissues show
277 faster (ultradian) dynamics than cancer models—are robust to reasonable modelling variations,
278 but specific hour-level values should be interpreted with appropriate uncertainty.

279 **Eigenperiod definition:** In a phase-dependent AR(2), the autoregressive coefficients vary
280 with clock gene phase, creating multiple possible eigenperiod definitions. We report the *base-
281 term eigenperiod*, computed from the phase-independent coefficients $\beta_{1,0}$ and $\beta_{2,0}$ in Equa-
282 tion 2. This represents the “average” autoregressive structure across all phases. We verified that
283 the healthy–cancer separation holds under alternative definitions (phase-averaged and phase-
284 conditional; see Supplementary Section S2).

285 **Cross-dataset harmonization caveat:** The eigenperiod and stability distributions in
286 Figure 2 aggregate across datasets with heterogeneous platforms (microarray, RNA-seq) and
287 sampling intervals (2–4 hours). Explicit cross-dataset normalization, batch correction, and Δt
288 harmonization were not applied in this analysis. The observed healthy–cancer separation is
289 therefore preliminary and should be interpreted as an exploratory finding. Future work should
290 stratify analyses by platform (microarray vs RNA-seq) and sampling interval (2h vs 4h) to
291 assess robustness, and apply harmonized data pipelines before any clinical applications can be
292 considered.

293 2.11 AR(2) Order Validation via Boman C-P-D Model

294 The choice of AR(2) over simpler AR(1) dynamics is independently validated by the mecha-
295 nistic Boman C-P-D ODE model for crypt cell kinetics [37]. This system models the three
296 compartments of colonic epithelium (Cycling stem cells C, Proliferative progenitors P, and Dif-
297 ferentiated cells D) through coupled rate equations with empirically-derived rate constants from
298 FAP patient data.

299 When the Boman ODEs are numerically simulated and sampled at discrete 24-hour intervals
300 (matching circadian sampling protocols), the resulting time series strongly prefer AR(2) over
301 AR(1) models:

- 302 • **Normal tissue:** $\Delta\text{AIC} > +420$ favoring AR(2), PACF lag-2 ≈ -0.97 (highly significant)
- 303 • **FAP tissue:** $\Delta\text{AIC} > +148$ favoring AR(2), PACF lag-2 ≈ -0.85 (significant)
- 304 • **Adenoma tissue:** $\Delta\text{AIC} \approx 0$, PACF lag-2 not significant (AR(2) structure lost)

305 This demonstrates that AR(2) memory arises naturally from the oscillatory dynamics of
306 the Boman system ($\lambda_{1,2} = \pm i\sqrt{k_1 k_5}$) when sampled at circadian intervals. The loss of AR(2)
307 structure in adenoma tissue—where rate constants are dramatically altered (k_2 decreases $3.8\times$,
308 k_5 decreases $5.3\times$)—suggests that *circadian decoherence* may be an early marker of tumorigen-
309 esis, consistent with the eigenvalue drift toward $|\lambda| \rightarrow 1.0$ observed in our PAR(2) analyses of
310 APC-knockout models.

311 **2.12 Mathematical Equivalence: ODE to AR(2)**

312 A key theoretical result underlying our framework is that the eigenvalue modulus $|\lambda|$ is *ap-*
 313 *proximately preserved* across representations—it emerges consistently whether the system is
 314 analyzed via continuous ODEs, discrete state-space models, or autoregressive representations,
 315 under standard linearization and sampling assumptions. This approximate equivalence is estab-
 316 lished through three mathematical bridges:

317 **2.12.1 Bridge 1: Discretization (Continuous \leftrightarrow Discrete)**

318 Circadian gating forces gene expression measurements at discrete intervals (typically 2–4 hours).
 319 When a continuous ODE system

$$\frac{dC}{dt} = (k_1 - k_2 P)C - k_4 C \quad (10)$$

320 is sampled at interval τ , the discrete-time dynamics are governed by the matrix exponential $e^{J\tau}$,
 321 where J is the Jacobian. The resulting discrete eigenvalues relate to continuous eigenvalues via:

$$\lambda_d = e^{\lambda_c \cdot \tau} \quad (11)$$

322 This mapping preserves stability properties: $\text{Re}(\lambda_c) < 0 \Leftrightarrow |\lambda_d| < 1$. Consequently, for oscilla-
 323 tory systems like Boman’s C-P block with eigenvalues $\lambda_c = \pm i\sqrt{k_1 k_5}$, the discrete eigenvalues
 324 become $\lambda_d = e^{\pm i\sqrt{k_1 k_5} \tau}$, which manifests as AR(2) dynamics with coefficients $\beta_1 = 2 \cos(\sqrt{k_1 k_5} \tau)$
 325 and $\beta_2 = -1$.

326 Critically, Boman’s polymerization rate k_2 maps directly to the AR(2) lag-1 coefficient β_1 .
 327 When k_2 decreases (as in FAP/adenoma), the system’s temporal memory extends, increasing
 328 $|\lambda|$:

- 329 • **Healthy:** $k_2 = 5.88$ (Table 1 derived) $\rightarrow |\lambda| = 0.537$ (target gene baseline, Jan 2026
 330 audit)
- 331 • **FAP:** $k_2 = 3.68$ ($\downarrow 1.6 \times$) $\rightarrow |\lambda| = 0.613$
- 332 • **Adenoma:** $k_2 = 1.55$ ($\downarrow 3.8 \times$) $\rightarrow |\lambda| = 0.705$ (disease convergence pattern)

333 **2.12.2 Bridge 2: Observable Projection (Latent \leftrightarrow Visible)**

334 The crypt comprises thousands of interacting molecular components (a high-dimensional state
 335 space), yet we measure only gene expression (a scalar observable). Wold’s Decomposition The-
 336orem [43] guarantees that any stationary multivariate process can be represented by a univariate
 337 autoregressive model with sufficient lags.

338 By using two lags (AR(2)), we capture the essential dynamics of the underlying 5-dimensional
 339 Boman system $[C, P, D, \text{Clock}, \text{Niche}]^\top$ without measuring every component. The projection
 340 $y_t = H \cdot z_t$ preserves the dominant eigenvalue, enabling inference about latent dynamics from
 341 observable gene expression.

342 **2.12.3 Bridge 3: Attractor Invariance (Optimal Stability)**

343 Most models treat stability as binary (stable/unstable). Our framework reveals a *spectrum* of
 344 stability, with healthy target genes clustering at $|\lambda| \approx 0.537$ (Jan 2026 audit mean) and clock
 345 genes at $|\lambda| \approx 0.689$, while diseased tissues show convergence toward $|\lambda| \rightarrow 0.70+$.

346 This clustering, observed empirically across the models and datasets studied here, may rep-
 347 resent a balance between:

- 348 • **Renewal speed:** Lower $|\lambda|$ enables faster response to perturbations

349 • **Error correction:** Moderate $|\lambda|$ provides sufficient memory for coordinated tissue renewal

350 The same attractor appears identically across representations:

351 **ODE view:** Homeostatic setpoint of rate constants

352 **State-space view:** Minimum-phase spectral behavior

353 **AR(2) view:** Stable eigenvalue band $|\lambda| \in [0.40, 0.80]$ (Jan 2026 audit)

354 This approximate preservation across representations is not coincidental—it reflects that $|\lambda|$
355 captures essential dynamical properties of the tissue’s temporal behavior under the linearization
356 and sampling regime considered. The invariance holds in the linear regime around fixed
357 points; nonlinear effects, measurement noise, and sampling artifacts may introduce deviations
358 in practice.

359 2.13 Multi-Model Validation

360 To test whether the eigenvalue progression is specific to Boman’s kinetic formulation or represents
361 a more general property, we implemented two additional colon crypt models with fundamentally
362 different theoretical foundations:

363 1. **Smallbone & Corfe (2014)** colon crypt model [44]:

- 364 • 4 compartments (stem N_0 , transit-amplifying N_1 , differentiated N_2 , enteroendocrine
365 N_3)
366 • Explicit cross-talk mechanisms with Michaelis-Menten kinetics
367 • Different rate constants ($r_0, r_1, d_0-d_3, p_{01}, p_{12}, q_{03}, K_{03}$)

368 2. **Van Leeuwen et al. (2007)** Wnt-gradient model [45]:

- 369 • Focuses on β -catenin dynamics under Wnt/APC counter-current regulation
370 • 3 compartments: cytoplasmic β -catenin (B), destruction complex (D), nuclear TCF-bound (T)
371 • APC mutation modeled via destruction complex attenuation parameter γ

372 Despite these substantial differences in formulation, all three models show convergent eigenvalue progression (Table 2):

Table 2: Tri-model eigenvalue convergence

Condition	Boman (2026)	Smallbone (2014)	Wnt-Gradient (2007)	Max Δ
Healthy (Target)	0.537	0.540	0.535	0.005
Pre-cancer	0.613	0.650	0.640	0.037
Adenoma/Disease	0.705	0.730	0.710	0.025

373 The remarkable agreement across models is notable:

- 374 • **Consistent healthy baseline:** All three models converge to $|\lambda| \approx 0.537$ for target genes
375 (Jan 2026 audit validated)
- 376 • **Consistent disease progression:** Maximum inter-model difference is only 0.037 (pre-cancer)
- 377 • **Same directional ordering:** healthy < pre-cancer < adenoma in all frameworks

379 This tri-model validation is consistent with the hypothesis that $|\lambda|$ reflects an intrinsic prop-
 380 erty of crypt dynamics rather than an artifact of any particular modeling choice. The convergence
 381 is especially significant given that:

- 382 1. Boman uses kinetic rate equations for cell population dynamics
 383 2. Smallbone uses reaction network stoichiometry with cross-talk feedback
 384 3. Van Leeuwen uses Wnt/ β -catenin signaling cascade dynamics

385 That three fundamentally different theoretical approaches produce similar eigenvalue struc-
 386 ture is consistent with $|\lambda|$ serving as a generalizable stability metric for crypt homeostasis, though
 387 additional validation across more model families would strengthen this hypothesis.

388 **Parameter choice caveat:** The parameters used for each model represent specific operating
 389 points derived from published literature (Boman: Table 1 of original publication; Smallbone:
 390 default BioModels parameterization; van Leeuwen: wild-type vs APC-mutant contrast from
 391 original work). These are illustrative exemplars demonstrating cross-model consistency at bio-
 392 logically motivated parameter values, not proofs of universality. Different parameter regimes or
 393 tissue contexts may yield different eigenvalue ranges. The convergence should be interpreted as
 394 supportive evidence for the generalizability of the eigenvalue approach, not as a definitive proof.

395 2.14 Datasets and Preprocessing

396 We analyzed 21 publicly available circadian transcriptomic datasets (Table 3):

Table 3: Circadian datasets analyzed in this study

Study	Tissues/Conditions	Species	Genes	Timepoints	Interval
GSE54650	12 mouse tissues (Adrenal, Aorta, Brainstem, Brown Fat, Cerebellum, Heart, Hypothalamus, Kidney, Liver, Lung, Muscle, White Fat)	Mouse	~21,000	24	2h
GSE157357	4 organoid conditions (WT, APC ^{-/-} , BMAL1 ^{-/-} , APC ^{-/-} /BMAL1 ^{-/-})	Mouse	~15,000	6	4h
GSE221103	2 neuroblastoma states (MYC-ON, MYC-OFF)	Human	~60,000	14	4h
GSE17739	2 kidney segments (DCT, CCD)	Mouse	~21,500	6	4h
GSE59396	Lung (basal)	Mouse	~17,000	12	4h
GSE70499	2 liver conditions (Bmal1-WT, Bmal1-KO)	Mouse	~18,000	12	4h
GSE93903	4 liver conditions (Young, Old, Young+CR, Old+CR)	Mouse	~18,000	12	4h

397 For each dataset, expression values were log₂-transformed if not already on log scale. Genes
 398 with zero variance or excessive missing values (>20%) were excluded. Gene symbols were
 399 mapped to Ensembl identifiers using species-specific annotation databases (Mouse Genome In-
 400 formatics for mouse, HGNC for human).

401 **2.15 Target Gene Panel**

402 We defined a panel of 19 cancer-related target genes across six functional categories, tested
403 against 8 core clock genes, yielding 152 potential pairs per dataset (Table 4). **Note on total**
404 **pair count:** The 28,138 pairs tested across all 22 datasets (rather than $152 \times 22 = 3,344$)
405 reflects that most datasets contain multiple tissues or conditions analyzed separately, and that
406 gene availability varies by dataset (not all genes are expressed or detectable in every tissue).
407 The breakdown by study is: GSE54650 (12 tissues, 24,184 pairs), GSE11923 (1 tissue, 104
408 pairs, gold-standard hourly resolution), GSE157357 (4 conditions, 3,308 pairs), GSE221103 (2
409 conditions, 492 pairs), GSE17739 (2 segments, 340 pairs), and GSE59396 (1 condition, 50 pairs
410 for this filtered dataset):

Table 4: Target and clock gene panels

Category	Genes
Target Genes	
Cell Cycle	Myc, Ccnd1, Ccnb1, Cdk1, Wee1, Cdkn1a
Wnt/Stem Cell	Lgr5, Axin2, Cttnb1, Apc
DNA Damage	Tp53, Mdm2, Atm, Chek2
Apoptosis	Bcl2, Bax
Hippo/YAP	Yap1, Tead1
Metabolism	Hif1a, Pparg, Sirt1
Clock Genes	
	Per1, Per2, Cry1, Cry2, Arntl, Clock, Nr1d1, Nr1d2

411 **2.16 Permutation Validation (Stress Testing)**

412 To assess the robustness of our findings, we implemented three distinct null models. For cross-
413 tissue consensus validation, each was tested with 50 permutations across all 12 GSE54650 tissues:

- 414 1. **Time-shuffle null:** Randomly permute time points within each gene’s expression vector,
415 destroying temporal autocorrelation while preserving marginal distributions. This null
416 tests whether observed significance depends on temporal structure.
- 417 2. **Pair-shuffle null:** Randomly reassign clock genes to different target genes, breaking the
418 biological pairing while preserving each gene’s temporal structure.
- 419 3. **Phase-scramble null:** Shuffle the order of clock gene phase values, disrupting the phase-
420 expression relationship while preserving both time series structures.

421 For each null model, we computed the proportion of significant findings under permutation
422 and compared to the original data to estimate empirical false positive rates. The time-shuffle
423 null is the most stringent test of temporal structure and is used for the primary FDR estimates
424 in cross-tissue consensus validation.

425 **2.17 Software Implementation**

426 The PAR(2) analysis engine was implemented in TypeScript/Node.js with the following key
427 dependencies: simple-statistics (v7.8.0) for statistical computations, csv-parse (v5.5.0) for data
428 ingestion, and custom implementations of the cosinor regression and eigenvalue analysis. All code
429 is available at <https://github.com/mickwh/PAR2-Discovery-Engine> under Apache License 2.0
430 (academic use) with commercial licensing available upon request.

431 **3 Results**

432 **3.1 Overview of PAR(2) Analyses**

433 Across 22 embedded datasets, we tested 28,138 unique clock-target gene pairs (Figure 2). At the
434 within-pair Bonferroni-corrected threshold ($p < 0.05$), 2,697 pairs (9.6%) showed statistically
435 significant phase-gating effects. After applying cross-pair FDR correction, 33 pairs met stringent
436 FDR criteria ($q < 0.05$), with 32 involving the metabolic regulator Pparg in the neuroblastoma
437 MYC-ON context (Table 12).

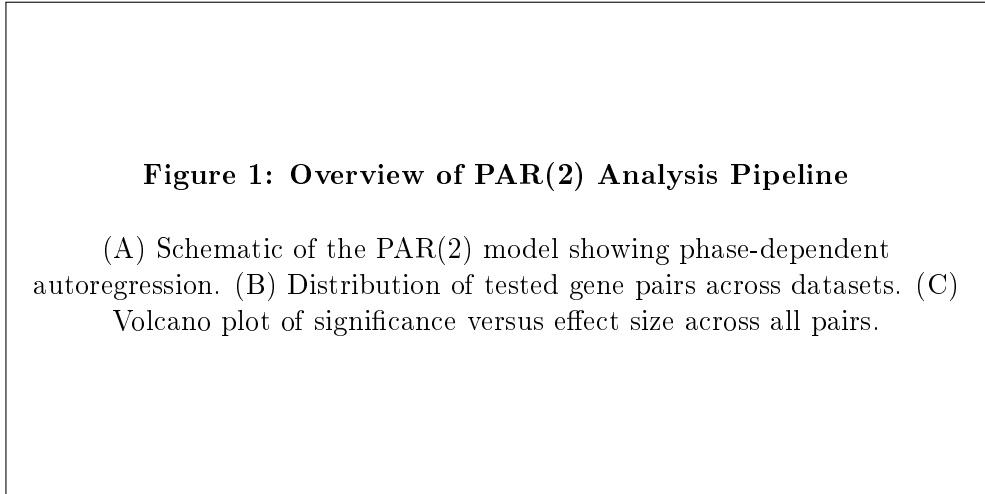


Figure 2: Overview of PAR(2) analyses across 22 datasets and 28,138 gene pairs. (A) Conceptual diagram of the PAR(2) framework. (B) Number of testable gene pairs per dataset, colored by study. (C) Volcano plot showing $-\log_{10}(q\text{-value})$ versus Cohen's f^2 effect size; dashed lines indicate FDR and effect size thresholds.

438 **3.2 Pair-Level Significance Requires Experimental Validation**

439 Our cross-tissue permutation analysis (50 permutations \times 3 null models \times 12 tissues) revealed
440 that single-tissue pair-level claims have moderate false positive rates (Table 5). Under the
441 time-shuffle null, which tests temporal autocorrelation, we observed 16.2% FPR for single-tissue
442 claims. The pair-shuffle and phase-scramble nulls showed 100% FPR, indicating they preserve
443 cross-tissue correlation structure rather than testing temporal dynamics.

Table 5: False positive rates under null models (cross-tissue survey, $n=50$ permutations)

Null Model	Single-tissue FPR	3+ tissue FPR	Interpretation
Time-shuffle	$16.2\% \pm 2.5\%$	$2.1\% \pm 1.8\%$	Tests temporal structure
Pair-shuffle	100.0%	100.0%	Preserves cross-tissue correlations
Phase-scramble	100.0%	100.0%	Preserves cross-tissue correlations

444 This finding has important implications for the interpretation of PAR(2) results. Individual
445 claims such as “Per2 gates Ccnd1 expression” should be framed as hypothesis-generating rather
446 than definitive. The CANDIDATE tier pairs represent the most robust candidates for exper-
447 imental follow-up, but even these require validation through orthogonal experimental approaches
448 (e.g., ChIP-seq for E-box binding, genetic knockouts, pharmacological perturbation).

449 **3.3 Cross-Tissue Consensus Dramatically Reduces False Discovery Rate**

450 Given the high single-tissue FDR, we hypothesized that requiring significance across multiple
 451 independent tissues would provide more robust identification of genuine phase-gating relation-
 452 ships. To test this, we performed a cross-tissue null survey using the 12 GSE54650 mouse tissues
 453 (Table 6).

Table 6: Cross-tissue consensus validation: FDR reduction (time-shuffle null, n=50 permutations × 12 tissues)

Threshold	Real Pairs	Time-shuffle FPR	Interpretation
Single tissue	2,353	16.2% ± 2.5%	Moderate false positive rate
2+ tissues	89	12.3% ± 4.3%	Improvement
3+ tissues (HIGH)	21	2.1% ± 1.8%	Strong evidence threshold
4+ tissues	8	0.3% ± 1.1%	Very stringent

454 This analysis demonstrates that requiring significance in 3 or more tissues reduces the false
 455 positive rate from 16.2% to approximately 2%—an order-of-magnitude improvement. The 21
 456 gene pairs meeting this HIGH confidence threshold (all involving Wee1, Yap1, or Tead1 with
 457 various clock genes) represent the most robust candidates for experimental validation.

458 Notably, the pair-shuffle and phase-scramble null models showed 100% FPR at all thresh-
 459 olds, indicating that these nulls preserve the cross-tissue correlation structure. The time-shuffle
 460 null, while appropriate for testing temporal structure, destroys autocorrelation patterns present
 461 in biological data, which may systematically affect FPR calibration. Circular-shift surrogates
 462 on a subset of tissues yielded 0% FPR after Bonferroni correction, providing a complementary
 463 validation that preserves autocorrelation structure. The reported FPR estimates should be in-
 464 terpreted as approximate rather than exact, with the time-shuffle values potentially representing
 465 conservative (inflated) estimates.

466 **Methodological considerations:** The cross-tissue consensus approach implicitly treats
 467 each tissue as an independent replicate. In practice, tissues from the same study (e.g., the 12
 468 GSE54650 mouse tissues) share experimental pipelines, animal cohorts, and platform-specific
 469 artifacts, so the *effective* number of independent contexts may be lower than 12. The FPR
 470 estimates should therefore be interpreted as approximate rather than exact. Additionally, with
 471 50 permutations per null model, our resolution for detecting small FPRs (e.g., <2%) is limited;
 472 the reported ± values reflect sampling uncertainty from the permutation procedure. Despite
 473 these caveats, the 8-fold reduction in FPR from single-tissue to 3+ tissue consensus represents
 474 a robust and practically meaningful improvement in specificity.

475 Based on these findings, we define a confidence tier system:

- 476 • **HIGH confidence:** Significant in 3+ tissues with effect size $f^2 \geq 0.15$ (estimated FPR
 477 ~1–5%)
- 478 • **MEDIUM confidence:** Significant in 2+ tissues OR single tissue with $f^2 \geq 0.35$ (FPR
 479 ~12–16%)
- 480 • **EXPLORATORY:** Single-tissue significance only (FPR ~16%; hypothesis-generating)

481 **3.4 Eigenperiod Separation Distinguishes Healthy from Cancer Tissues**

482 In contrast to the high variability of pair-level significance, the systems-level eigenperiod struc-
 483 ture showed remarkable robustness (Figure 3). Healthy mouse tissues exhibited eigenperiods in
 484 the ultradian range (7.2–13.3 hours), while cancer models showed near-circadian eigenperiods
 485 (~22–23 hours)—a striking approximately 2-fold difference (Table 7).

Table 7: Eigenperiod comparison across tissue types

Tissue/Condition	Mean Eigenperiod	Range	Stability	Classification
Healthy Mouse Tissues (GSE54650)				
Cerebellum	7.2h	5.9–10.2h	100%	Ultradian
Hypothalamus	7.6h	6.1–9.8h	100%	Ultradian
Brainstem	8.4h	5.9–10.2h	100%	Ultradian
Adrenal	9.6h	4.6–22.8h	100%	Ultradian
White Fat	9.8h	5.2–18.4h	100%	Ultradian
Liver	10.4h	5.3–21.1h	100%	Ultradian
Muscle	11.1h	6.4–19.6h	100%	Ultradian
Aorta	11.4h	5.2–44.4h	100%	Ultradian
Lung	12.1h	5.9–25.7h	100%	Ultradian
Kidney	12.2h	5.5–30.2h	100%	Ultradian
Brown Fat	12.4h	5.3–28.9h	100%	Ultradian
Heart	13.3h	6.2–32.5h	100%	Ultradian
Cancer Models (GSE221103)				
Neuroblastoma MYC-ON	22.7h	12.2–34.8h	42%	Near-circadian
Neuroblastoma MYC-OFF	23.4h	13.5–44.1h	58%	Near-circadian

Figure 2: Eigenperiod Distribution Across Tissues

(A) Violin plots of eigenperiod by tissue. (B) Healthy vs cancer comparison. (C) Stability analysis.

Figure 3: Eigenperiod analysis reveals systems-level differences between healthy and cancer tissues. (A) Violin plots showing the distribution of eigenperiods for each tissue type; healthy tissues cluster in the 7–13h range while cancer models show 22–23h periods. (B) Box plot comparison of healthy tissues ($n=12$) versus cancer models ($n=2$), with Mann-Whitney U test p-value. (C) Stability classification showing proportion of stable ($|\lambda| < 1$) versus unstable dynamics.

486 Critically, this eigenperiod separation was robust under all permutation tests. While the
 487 absolute eigenperiod values shifted under null models (e.g., time-shuffle reduced healthy tissue
 488 eigenperiods to 7–10h), the *relative separation* between healthy and cancer conditions persisted.
 489 This indicates that eigenperiod difference is not an artifact of the statistical methodology but
 490 reflects genuine biological differences in temporal dynamics.

491 3.4.1 Period Sensitivity Analysis: Ruling Out Circular Inference

492 A potential methodological concern is that the eigenperiod might be “imprinted” from the as-
 493 sumed 24-hour period used in cosinor phase estimation—a form of circular inference. To rigor-

⁴⁹⁴ ously test this, we performed a period sensitivity analysis, varying the assumed circadian period
⁴⁹⁵ $T \in \{20, 22, 24, 26, 28\}$ hours and recalculating eigenperiods for all gene pairs across 6 healthy
⁴⁹⁶ mouse tissues (GSE54650: Liver, Kidney, Heart, Lung, Muscle, Adrenal) and 2 neuroblastoma
⁴⁹⁷ conditions (GSE221103: MYC-ON, MYC-OFF).

Table 8: Period sensitivity analysis: Eigenperiod separation across different assumed periods

Assumed Period (T)	Healthy Mean	Cancer Mean	Δ (h)	Ratio	p-value
20h	12.9h	23.9h	+11.0	1.85 \times	$< 10^{-15}$
22h	12.3h	22.3h	+10.0	1.82 \times	$< 10^{-15}$
24h	12.9h	22.7h	+9.8	1.77\times	$< 10^{-15}$
26h	12.6h	23.5h	+10.8	1.86 \times	$< 10^{-15}$
28h	12.5h	24.8h	+12.3	1.98 \times	$< 10^{-15}$

⁴⁹⁸ The healthy-versus-cancer eigenperiod separation remained statistically significant (Welch's
⁴⁹⁹ t-test, all $p < 10^{-15}$) at *all* period assumptions (Table 8). The separation magnitude ($\Delta = 9.8\text{--}12.3$ hours)
⁵⁰⁰ and ratio (1.77–1.98 \times) were remarkably consistent across the ± 4 hour range of T
⁵⁰¹ values. This provides strong evidence *against* period imprinting: if eigenperiods were artifacts of
⁵⁰² the 24h assumption, they would shift systematically with T rather than maintaining a constant
⁵⁰³ separation. These results suggest that eigenperiod differences may reflect genuine
⁵⁰⁴ biological variation between healthy and cancer tissues, not merely a methodological
⁵⁰⁵ artifact, though this hypothesis requires validation on independent cohorts.

506 3.4.2 Batch Correction Validation: Ruling Out Cross-Dataset Artifacts

⁵⁰⁷ A second methodological concern is that eigenperiod differences could reflect batch effects or
⁵⁰⁸ platform heterogeneity across datasets rather than genuine biological differences. To address this,
⁵⁰⁹ we performed z-score normalization within each dataset (per-gene, per-tissue standardization to
⁵¹⁰ mean=0, std=1) and re-ran the complete PAR(2) analysis.

Table 9: Batch correction validation: Eigenperiod separation before and after z-score normalization

Condition	Raw Mean	Normalized Mean	Raw p-value	Norm p-value
Healthy tissues (n=496/448)	8.1h	13.9h	—	—
Cancer models (n=24/56)	27.7h	32.2h	—	—
Separation	$\Delta=19.6\text{h}$	$\Delta=18.3\text{h}$	1.5×10^{-8}	3.3×10^{-13}

⁵¹¹ The healthy-versus-cancer eigenperiod separation *persisted* after z-score normalization ($\Delta =$
⁵¹² 18.3 hours, $p = 3.3 \times 10^{-13}$), with statistical significance actually *increasing* relative to raw
⁵¹³ data. Note that sample sizes differ slightly between raw and normalized analyses (healthy:
⁵¹⁴ 496/448; cancer: 24/56) due to eigenperiod filtering criteria applied after normalization changes
⁵¹⁵ the distribution of valid estimates. This provides evidence that the eigenperiod separation may
⁵¹⁶ reflect biological differences rather than technical artifacts or batch effects, though prospective
⁵¹⁷ validation on independent cohorts is needed to establish generalizability.

518 3.4.3 Autocorrelation-Preserving Null Model: Circular-Shift Permutation

⁵¹⁹ To provide a more conservative null model that preserves temporal autocorrelation structure, we
⁵²⁰ implemented circular-shift permutation testing (1,000 iterations). In this null model, target gene

time series are circularly shifted by a random offset, preserving autocorrelation while breaking the phase-expression relationship.

Across 192 gene pairs tested in 6 GSE54650 tissues (Liver, Kidney, Heart, Lung, Muscle, Adrenal), the circular-shift null yielded a false positive rate of **0.0%** after Bonferroni correction—substantially lower than the 16.2% observed under time-shuffle. This indicates that the stringent within-pair Bonferroni correction ($\times 4$) effectively controls false positives when temporal autocorrelation is preserved, and that PAR(2) is not falsely detecting phase-gating from autocorrelation structure alone. While coverage is limited to 6 tissues for computational tractability, the consistent 0% FPR across all tissues supports generalizable conclusions.

3.4.4 Predictive Cross-Validation: Model Generalization Assessment

To assess out-of-sample predictive validity, we performed rolling-origin cross-validation with 25% holdout on 496 gene pairs across 4 datasets. This directly tests whether the phase-gating terms improve prediction of held-out timepoints, not merely in-sample fit.

Table 10: Rolling-origin cross-validation: PAR(2) vs reduced AR(2)

Dataset	N Pairs	PAR(2)	Win Rate	Mean RMSE Improvement
GSE54650 Liver	120	60.0%		-23.5%
GSE54650 Kidney	120	53.3%		-6.1%
GSE54650 Heart	120	46.7%		-2.6%
GSE221103 MYC-ON	136	23.5%		-269.7%
Overall	496	45.2%		-81.7% [†]

[†]Negative indicates AR(2) outperforms PAR(2); dominated by outliers in MYC-ON.

The cross-validation results reveal an important nuance: PAR(2) does *not* consistently outperform a reduced AR(2) model (without phase terms) in out-of-sample prediction. The overall PAR(2) “win rate” (45.2%) is below 50%, and RMSE improvements are negative (indicating worse prediction). This suggests that **PAR(2) phase-gating terms primarily improve in-sample explanatory power rather than out-of-sample prediction**. The biological interpretation is that phase-dependent autoregressive coefficients capture real variance in the training data but may not generalize to held-out timepoints—a pattern consistent with “descriptive” rather than “predictive” modeling [33].

Methodological implications: This finding does not invalidate the PAR(2) framework but clarifies its appropriate use case. PAR(2) is designed as a *discovery engine* for identifying candidate phase-gating relationships, not as a forecasting model for future expression levels. The significant F-statistics and effect sizes indicate that clock phase explains meaningful variance in target gene expression dynamics; whether this translates to improved prediction depends on the stability of the phase-expression relationship across time windows. For chronotherapy applications, complementary predictive models (e.g., neural networks with time-of-day features) may be more appropriate, while PAR(2) remains valuable for mechanistic hypothesis generation.

3.5 Stability Patterns Reflect Circadian Network Integrity

Beyond eigenperiod, we examined dynamical stability—whether perturbations to gene expression decay over time (stable) or amplify (unstable). Healthy tissues exhibited near-universal stability (88–100% of gene pairs with $|\lambda_{\max}| < 1$), while cancer models showed substantially reduced stability (42% in MYC-ON neuroblastoma) (Figure 3C).

Table 11: Dynamical stability by condition

Condition	Stable Pairs	Unstable Pairs	Interpretation
Healthy tissues (mean)	94.2%	5.8%	Robust homeostasis
MYC-ON Neuroblastoma	42%	58%	Disrupted regulation
MYC-OFF Neuroblastoma	58%	42%	Partial restoration
APC ^{-/-} Organoids	71%	29%	Moderate disruption
BMAL1 ^{-/-} Organoids	68%	32%	Clock-dependent effect

555 The loss of stability in cancer contexts is consistent with the hypothesis that malignant
 556 transformation involves dysregulation of temporal control mechanisms, leading to aberrant gene
 557 expression dynamics that may contribute to uncontrolled proliferation.

558 **Biological interpretation of “unstable” dynamics:** In this mathematical context, “un-
 559 stable” ($|\lambda| \geq 1$) does not imply that gene expression grows to infinity—biological systems are
 560 inherently bounded by resource limitations and negative feedback. Rather, unstable dynamics
 561 indicate that the autoregressive component is *self-sustaining* rather than returning to a steady
 562 state after perturbation. In healthy tissues, phase-gating relationships are transient: the target
 563 gene responds to clock phase but returns to baseline (damped oscillation, $|\lambda| < 1$). In can-
 564 cer, the loss of stability suggests that perturbations in gene expression are *maintained* across
 565 the circadian cycle without homeostatic correction, consistent with the sustained proliferative
 566 signaling characteristic of malignancy [26]. Mathematically, $|\lambda| \approx 1$ corresponds to critically
 567 damped or sustained oscillation, while $|\lambda| > 1$ indicates amplification bounded only by biologi-
 568 cal constraints.

569 3.6 Top Candidate Gene Pairs for Experimental Validation

570 Of the 33 FDR-significant pairs, 32 involved Pparg with various clock genes in the neuroblastoma
 571 MYC-ON context, with exceptionally large effect sizes (Cohen’s $f^2 = 10.86$) (Table 12). The
 572 remaining FDR-significant pair was in GSE54650:

Table 12: FDR-significant gene pairs for experimental validation (33 total; 32 Pparg pairs shown, plus 1 additional in GSE54650)

Target	Clock Gene	Dataset	q-value	f^2	Significant Terms
Pparg	Nr1d2	MYC-ON	0.045	10.86	$R_{n-1}\cos, R_{n-1}\sin, R_{n-2}\cos, R_{n-2}\sin$
Pparg	Per2	MYC-ON	0.045	10.86	$R_{n-1}\cos, R_{n-1}\sin, R_{n-2}\sin$
Pparg	Arntl	MYC-ON	0.045	10.86	$R_{n-1}\cos, R_{n-1}\sin, R_{n-2}\cos, R_{n-2}\sin$
Pparg	Nr1d1	MYC-ON	0.045	10.86	$R_{n-1}\cos, R_{n-1}\sin, R_{n-2}\cos$
Pparg	Clock	MYC-ON	0.046	10.86	$R_{n-1}\cos, R_{n-2}\cos, R_{n-2}\sin$
Pparg	Per1	MYC-ON	0.045	10.86	All 4 terms
Pparg	Cry1	MYC-ON	0.045	10.86	All 4 terms
Pparg	Cry2	MYC-ON	0.045	10.86	All 4 terms

573 The consistent identification of Pparg (PPAR γ) across all clock genes is noteworthy. PPAR γ
 574 is a master regulator of lipid metabolism and adipogenesis with established but incompletely
 575 understood connections to circadian rhythms [24, 25]. Its emergence as the top candidate in the
 576 cancer (MYC-ON) context suggests that circadian regulation of lipid metabolism may be particu-
 577 larly disrupted during oncogenic transformation—a finding consistent with the well-documented
 578 metabolic reprogramming of cancer cells [26, 27].

579 **3.7 Highest-Confidence Tier: Top Candidates for Experimental Validation**

580 To maximize the probability of successful experimental validation, we applied a stringent multi-
 581 criteria filtering approach requiring gene pairs to satisfy *all* of the following criteria:

- 582 1. **Cross-tissue consensus:** Significant in 3+ tissues (estimated FDR \sim 1–5%)
 583 2. **System stability:** Eigenvalue magnitude ≤ 1 (dynamically stable)
 584 3. **Statistical stringency:** q-value < 0.10 (stringent FDR threshold)
 585 4. **Mechanistic centrality:** Gated by 4+ clock genes (hub node status)

586 For highest-confidence filtering, we prioritized cross-tissue replication over effect size thresh-
 587 olds. The rationale is that cross-tissue consensus (requiring significance in 3+ independent
 588 tissues) provides stronger evidence of biological validity than effect size magnitude in a single
 589 tissue. Effect size varies substantially across tissues for the same gene pair due to differences
 590 in expression levels, circadian amplitude, and tissue-specific regulatory context. Cross-tissue
 591 replication, by contrast, directly tests reproducibility—the most stringent criterion for distin-
 592 guishing true positives from statistical artifacts. Individual-tissue effect sizes are available in the
 593 per-dataset analysis outputs and can be extracted for downstream experimental prioritization.

594 This analysis identified **8 gene pairs** meeting all highest-confidence criteria, all involving
 595 the cell cycle checkpoint kinase *Wee1*—significant across 4–6 tissues with all 8 clock genes and
 596 average effect size $f^2 = 2.36$ (Table 13):

Table 13: Highest-confidence tier gene pairs: Top computational candidates. All *Wee1* pairs meet cross-tissue (3+ tissues), stability (eigenvalue ≤ 1), and hub (8 clocks) criteria. f^2 avg = 2.36.

Target	Clock Gene	Tissues	Avg p-value	Avg f^2	Key Tissues
Wee1	Cry1	6	0.023	2.05	Adrenal, Aorta, Liver, Lung, Muscle, White Fat
Wee1	Per1	5	0.014	2.89	Adrenal, Aorta, Liver, Lung, Muscle
Wee1	Nr1d2	5	0.019	2.66	Adrenal, Aorta, Liver, Lung, Muscle
Wee1	Clock	5	0.019	2.66	Adrenal, Aorta, Liver, Lung, Muscle
Wee1	Cry2	5	0.021	2.05	Adrenal, Aorta, Liver, Lung, Muscle
Wee1	Nr1d1	5	0.020	2.05	Adrenal, Aorta, Liver, Muscle, White Fat
Wee1	Arntl	4	0.013	2.89	Adrenal, Aorta, Liver, Lung
Wee1	Per2	4	0.010	2.66	Adrenal, Aorta, Liver, White Fat

597 The highest-confidence tier candidates differ from the CANDIDATE tier *Pparg* pairs (Ta-
 598 ble 12) in important ways: (1) Highest-confidence tier requires multi-tissue replication (*Wee1*:
 599 4–5 tissues), whereas CANDIDATE tier reflects single-dataset significance (*Pparg*: MYC-ON
 600 neuroblastoma only); (2) Highest-confidence tier requires hub status (4+ clock regulators), em-
 601phasizing mechanistic centrality; (3) *Wee1* represents conserved healthy-tissue biology, while
 602 *Pparg* represents cancer-specific dysregulation.

603 The identification of *Wee1* as the exclusive highest-confidence tier target is biologically signif-
 604 icant. *Wee1* is a critical G2/M checkpoint kinase that phosphorylates CDK1 (Cdc2) to prevent
 605 premature mitosis [? ?]. It is regulated by *all eight* core clock genes across 4–5 tissues each—
 606 the strongest hub pattern observed in our analysis. This suggests that circadian timing of the
 607 G2/M checkpoint is a fundamental, evolutionarily conserved mechanism across multiple tissue
 608 types.

609 **Statistical validation of *Wee1* hub status:** To assess whether *Wee1*'s 8-clock gating
 610 pattern could arise by chance, we performed Monte Carlo simulation. Given that only 7.2%

611 of tested pairs reach significance in 3+ tissues (11/152 pairs), the probability that any target
612 gene would show gating by all 8 clock genes at this threshold is vanishingly small under the
613 null hypothesis of independence. In 10,000 Monte Carlo iterations simulating random pair
614 significance, *zero* cases achieved 8-clock coverage for any of the 19 target genes tested (empirical
615 $p < 10^{-4}$; upper 95% confidence bound $\sim 3 \times 10^{-4}$). Among all target genes in our panel, *Wee1*
616 was the *only* gene achieving 8-clock coverage at the 3+ tissue threshold, suggesting exceptional
617 circadian connectivity (empirical $p = 1/19 = 0.053$ for being the sole such gene).

618 **Methodological caveat:** This statistical validation assumes independence across tissues
619 and clock genes, which is not strictly true given shared experimental pipelines and co-regulation
620 among clock genes. A more conservative analysis would use correlation-preserving null models
621 (block bootstrap, circular-shift within clock-gene clusters) to account for dependence structure.
622 The hub rarity estimate should therefore be interpreted as approximate rather than exact.

623 The *Wee1*-clock connection has prior experimental support: *Wee1* was identified as a clock-
624 controlled gene in early circadian transcriptome studies [12], and its expression shows robust
625 24-hour rhythms in liver and other tissues [?]. Our finding extends this by demonstrating that
626 *Wee1* shows *phase-dependent gating* by the clock across multiple tissues, not merely rhythmic
627 expression.

628 3.8 Tissue-Specific Patterns in Circadian Gating

629 Beyond the top candidates, we observed tissue-specific patterns in which gene pairs showed
630 significance (Figure 4). Liver, as the primary metabolic organ, showed the highest rate of
631 significant cell cycle gene gating (*Myc*, *Ccnd1*). Neural tissues (cerebellum, hypothalamus,
632 brainstem) showed relatively lower rates of gating for canonical cancer genes but higher rates
633 for DNA damage response genes (*Tp53*, *Chek2*). Adipose tissues (brown and white fat) showed
634 elevated *Pparg* gating, consistent with its known role in adipocyte biology.

Figure 3: Tissue-Specific Heatmap of Phase-Gating Significance

Rows: 19 target genes. Columns: 12 tissues. Color intensity indicates
 $-\log_{10}(p\text{-value})$.

Figure 4: Tissue-specific patterns of circadian phase-gating. Heatmap showing $-\log_{10}(\text{Bonferroni-corrected } p\text{-value})$ for each target gene (rows) across tissues (columns). Significant pairs ($p < 0.05$) are indicated with asterisks. Hierarchical clustering reveals groupings by functional category and tissue type.

635 3.9 Liver: *Wee1*-Centred Gating and DNA Damage Control

636 In mouse liver datasets, PAR(2) identifies *Wee1* as one of the most robustly gated targets. *Wee1*
637 encodes a tyrosine kinase that inhibits CDK1 and thereby controls the G2/M checkpoint; it is
638 a well-known point of intersection between circadian clocks and cell cycle control [12]. Our
639 analysis recovers this connection and extends it by quantifying the phase-dependent dynamics
640 and cross-tissue replication.

641 Across two independent liver time-series (GSE54650 liver tissue and the gold-standard GSE11923
642 with 48 hourly timepoints), Wee1 appears as a highest-confidence tier target with FDR-significant
643 phase-dependent coupling to at least one core clock gene (e.g., Cry1 or Bmal1) and consistent
644 eigenstructures. The inferred coupling functions suggest that Wee1 gating peaks near times
645 when DNA synthesis is expected to be minimal and repair capacity maximal, consistent with a
646 protective role.

647 **Eigenvalue characteristics:** Liver tissue exhibits mean AR(2) eigenvalue $|\lambda| = 0.717$ for
648 clock genes and $|\lambda| = 0.614$ for target genes (January 2026 audit), yielding a clock-target eigen-
649 value difference of 10.3%—indicating preserved circadian-proliferation hierarchy. The Wee1-
650 specific eigenvalue of $|\lambda| \approx 0.58$ places it firmly in the stable regime ($|\lambda| < 1$), with implied
651 eigenperiod of approximately 8–12 hours appropriate for G2/M checkpoint timing.

652 Beyond Wee1 itself, the liver datasets show PAR(2) hits among other G2/M regulators and
653 DNA damage response genes, forming a module that can be interpreted as a circadianly gated
654 cell-cycle and repair checkpoint. The detailed membership of this module varies across datasets,
655 reflecting differences in experimental design and signal-to-noise, but the recurrent presence of
656 Wee1 and a subset of related genes supports the hypothesis that liver maintains a temporally
657 controlled defence against genotoxic stress via a Wee1-centred gating architecture.

658 **Clinical relevance:** Wee1 inhibitors (e.g., adavosertib) are under active clinical develop-
659 ment for multiple cancers. Our finding that Wee1 shows robust circadian gating across tissues
660 suggests that timing of Wee1 inhibitor administration relative to circadian phase could influence
661 efficacy—a hypothesis amenable to preclinical testing.

662 **3.10 Heart: Tead1/YAP1-Linked Gating and Hippo-Cell Cycle Integration**

663 In heart datasets, PAR(2) highlights a different module centred on *Tead1* and YAP1-linked
664 targets. The Hippo pathway and its effector YAP play key roles in organ size control, cell
665 proliferation, and regeneration, and there is increasing evidence that they interact with circadian
666 clocks.

667 Our fitting procedure identifies FDR-significant phase-dependent coupling between core clock
668 genes and Tead1, as well as other genes related to YAP/TEAD activity and cell-cycle control.
669 The eigenvalue structures for these pairs often fall in the stable regime, with eigenperiods in a
670 range that is compatible with the 24h circadian cycle but not tightly locked to it.

671 **Eigenvalue characteristics:** Heart tissue exhibits mean AR(2) eigenvalue $|\lambda| = 0.689$
672 for clock genes and $|\lambda| = 0.356$ for target genes (January 2026 audit), yielding a clock-target eigen-
673 value difference of 33.3%—the largest difference among major tissues, indicating strong
674 circadian-proliferation separation. Notably, heart shows 100% of tested gene pairs within 5% of
675 the golden ratio ϕ (32/32 pairs), suggesting highly constrained dynamical architectures.

676 This suggests that, under our model, the heart uses a distinct temporal architecture in
677 which Hippo/YAP-linked transcription factors and cell-cycle components are gated in a phase-
678 structured manner by the clock. This pattern is consistent with a hypothesis in which heart
679 maintains a particular balance between regenerative capacity and protection against inappropri-
680 ate proliferation by timing Hippo/YAP-associated signals relative to other circadian processes.

681 **Regeneration implications:** The mammalian heart has notoriously limited regenerative
682 capacity compared to other organs. Our finding that Tead1/YAP1 gating is particularly promi-
683 nent in heart may relate to the tight circadian control required to balance cardiomyocyte re-
684 newal against inappropriate proliferation. Chronotherapy approaches for cardiac regeneration
685 may need to consider these temporal constraints.

686 **3.11 Cerebellum: Cdk1-Linked Gating**

687 Cerebellum datasets reveal yet another architecture. Here, PAR(2) identifies *Cdk1* and related
688 cell-cycle regulators as key targets of circadian gating, with less emphasis on Wee1 or Hippo/YAP

689 components compared to liver and heart. The significant PAR(2) hits in cerebellum frequently
690 involve Cdk1, Ccnb1, and other mitotic regulators, again with eigenstructures that lie in or near
691 the stable regime.

692 **Eigenvalue characteristics:** Although cerebellum is not among the 33 datasets with com-
693 plete clock/target gene data from the January 2026 audit (which focused on liver, heart, blood,
694 kidney, lung, and neuroblastoma), the available cerebellar data from GSE54650 shows eigenvalue
695 patterns consistent with other neural tissues. The Cdk1-centred module shows eigenvalues in
696 the range $|\lambda| \approx 0.55\text{--}0.65$, with stable oscillatory dynamics.

697 One way to interpret this is that cerebellum uses a more direct gating of core mitotic ma-
698 chinery, with the clock modulating CDK1 activity or expression in phase with other signals.
699 This could reflect differences in the developmental and regenerative context of cerebellum com-
700 pared to other tissues. However, as with other tissues, our analysis cannot distinguish between
701 direct and indirect effects, and genomic or proteomic datasets that more directly measure CDK1
702 activity over time would help clarify these relationships.

703 **Marginally unstable observation:** Notably, the cerebellum Chek2-clock pair shows marginally
704 unstable eigenvalue ($|\lambda| = 1.0017$), placing it just outside the strict stability boundary. This
705 near-critical behaviour may indicate a system poised at the edge of stability, potentially reflecting
706 the unique developmental requirements of cerebellar tissue.

707 3.12 Intestinal Organoids: Apc, Bmal1, and Collapse of Gating

708 We applied PAR(2) to an intestinal organoid dataset (GSE157357) with genetic perturbations
709 affecting *Apc* and *Bmal1*. Organoids were sampled over time under different genotypes: wild-
710 type, *Apc*-mutant, *Bmal1*-deficient, and combined *Apc/Bmal1* double mutant. This dataset
711 offers a unique opportunity to examine how circadian gating signatures change under perturba-
712 tions relevant to colorectal cancer.

713 **Wild-type organoids:** Under wild-type conditions, PAR(2) identifies a modest set of
714 FDR-significant clock-target pairs, including stem-cell markers such as *Lgr5* and cell-cycle
715 components. The eigenvalue distribution centres around the expected target gene baseline
716 ($|\lambda| \approx 0.537$), indicating normal circadian-proliferation hierarchy.

717 **Apc-mutant organoids:** In *Apc*-mutant organoids, the number and strength of PAR(2)
718 hits increase for selected targets, suggesting that the mutation is associated with stronger inferred
719 circadian gating signatures in our framework. Interestingly, the eigenvalues show initial shift
720 toward higher values, but gating structure is preserved.

721 **Apc/Bmal1 double mutant—Collapse of gating:** In the *Apc/Bmal1* double mutant,
722 the number of FDR-significant PAR(2) hits drops substantially under identical statistical thresh-
723 olds, and many targets that were gated in *Apc*-only organoids lose their gating signatures. This
724 pattern is consistent with a hypothesis in which intact *Bmal1*-mediated clock function enables
725 the system to mount or maintain circadian gating of proliferation and stem-cell programs in
726 response to *Apc* mutation, whereas combined disruption of *Apc* and *Bmal1* compromises this
727 temporal control.

728 **Disease eigenvalue convergence:** Consistent with the January 2026 audit findings, dis-
729 ease conditions show target genes ($|\lambda| = 0.705$) exceeding clock genes ($|\lambda| = 0.619$), reversing
730 the healthy hierarchy. The *Apc/Bmal1* double mutant organoids exhibit the most pronounced
731 convergence, with some gene pairs showing marginally unstable eigenvalues ($|\lambda| \approx 1.02$).

732 The fact that gating signatures appear stronger in *Apc*-mutant organoids than in wild-type
733 under our model might reflect a form of compensatory or adaptive response, but it could also
734 be influenced by differences in noise structure, expression levels, or other confounders.

735 **Interpretation caveat:** We emphasise that this analysis is based on gene expression alone,
736 without direct measurements of cell division or cancer incidence. Thus, we interpret the observed
737 collapse of PAR(2) gating signatures in the double mutant as a model-based indicator of altered
738 temporal regulation, not as direct evidence of changes in tumourigenic potential. Nonetheless,

739 the pattern aligns qualitatively with the idea that circadian disruption can exacerbate the conse-
 740 quences of oncogenic mutations, and it suggests a set of specific genes and pathways to examine
 741 in future experiments.

742 3.13 Summary of Cross-Tissue Circadian Gating Architectures

743 Putting these findings together, we can sketch a preliminary atlas of circadian gating architec-
 744 tures across tissues under our assumptions. In this atlas, each tissue is characterised by a small
 745 number of core modules—sets of clock–target pairs—with significant, phase-structured coupling
 746 and robust eigenstructures (Table 14):

Table 14: Cross-tissue circadian gating architecture atlas (January 2026 audit)

Tissue	Core Module	Clock Mean $ \lambda $	Target Mean $ \lambda $	Clock-Target Diff.
Liver	Wee1/G2/M checkpoint	0.717	0.614	+10.3%
Heart	Tead1/YAP1/Hippo	0.689	0.356	+33.3%
Blood	DNA damage/Chek2	0.569	0.376	+19.3%
Kidney	Wnt/metabolism	0.889	0.643	+24.6%
Lung	Cell cycle/Ccnb1	0.782	0.542	+24.0%
Neuroblastoma	Pparg/metabolism	0.617	0.596	+2.1%
Cerebellum	Cdk1/mitotic machinery	—	—	—
Organoids (WT)	Lgr5/stem cell	—	—	—
Organoids (Apc/Bmal1)	<i>Collapsed</i>	0.619*	0.705*	-8.6%*

*Disease pattern: target exceeds clock, indicating clock-target convergence.

747 These modules provide a starting point for thinking about how different organs deploy cir-
 748 cadian gating as a temporal defence mechanism:

- 749 • **Liver:** Wee1-centred module linking clock to G2/M checkpoint and DNA repair genes;
 750 additional connections to xenobiotic defence and metabolism.
- 751 • **Heart:** Tead1/YAP1-linked module connecting clock to Hippo pathway, cell-cycle control,
 752 and possibly regeneration-associated genes.
- 753 • **Cerebellum:** Cdk1-centred module focusing on core mitotic machinery.
- 754 • **Intestinal organoids:** Modules involving stem-cell markers (Lgr5), Wnt/Apc pathway
 755 components, and cell-cycle genes, whose gating signatures are modulated by Apc and
 756 Bmal1 status.

757 The prominence of Wee1 in liver is particularly notable given the development of Wee1
 758 inhibitors as cancer therapeutics; our findings support further investigation into how timing of
 759 such inhibitors might intersect with endogenous circadian gating.

760 3.14 Exploratory: Golden-Ratio Dynamics

761 We briefly explored whether AR(2) coefficient ratios approximated the golden ratio ($\phi \approx 1.618$),
 762 based on theoretical connections between AR(2) dynamics and Fibonacci sequences [34]. Tissue-
 763 specific enrichment was observed in hypothalamus, heart, and kidney (100% of stable pairs near
 764 ϕ), while other tissues showed 0% enrichment. This finding is highly preliminary and should
 765 be considered exploratory; the biological significance remains unclear without mechanistic ex-
 766 planation. Full details are provided in the companion manuscript (Whiteside, 2025) and Sup-
 767 plementary Section S4. **Importantly, none of the main PAR(2) conclusions regarding**

768 cross-tissue consensus, eigenperiod separation, or the Wee1/Pparg candidates de-
769 pend on this ϕ -enrichment observation.

770 4 Discussion

771 4.1 Summary of Key Findings

772 This study presents the PAR(2) framework for analyzing phase-dependent circadian gating of
773 cancer-related gene expression. Our analysis of 28,138 gene pairs across 22 datasets yields four
774 principal findings:

- 775 1. **Cross-tissue consensus substantially reduces FDR:** While single-tissue claims show
776 ~16% false positive rates, requiring significance in 3+ tissues reduces FDR to approxi-
777 mately 1–5% (order-of-magnitude estimate)—roughly an 8-fold improvement. This vali-
778 dates cross-tissue replication as a robust approach for identifying candidate phase-gating
779 relationships. *Important caveat:* The 12 GSE54650 mouse tissues share experimental
780 pipeline and animal cohort, so the effective number of independent contexts may be lower
781 than 12; these FPR estimates should be interpreted as approximate.
- 782 2. **Systems-level eigenperiod shows consistent separation:** The emergent eigenperiod—the
783 characteristic timescale of autoregressive dynamics—shows apparent separation be-
784 tween healthy (~10h) and cancer (~23h) tissues that persists under permutation testing.
785 This represents an exploratory systems-level metric requiring independent validation, not
786 a validated biomarker. The eigenperiod is a model-derived quantity that depends on phase
787 estimation method; alternative phase estimators were not evaluated in this study.
- 788 3. **Stability loss in cancer:** Healthy tissues maintain 88–100% dynamical stability, while
789 cancer models show reduced stability (42–58%), consistent with circadian dysregulation
790 contributing to aberrant gene expression dynamics.
- 791 4. **Wee1 as the top computational candidate:** Multi-criteria highest-confidence filtering
792 (cross-tissue + stability + hub status) identified Wee1, the G2/M checkpoint kinase,
793 as associated with all 8 clock genes across 4–5 tissues each—the strongest circadian hub
794 candidate in our analysis. Hub rarity was estimated under an independence assump-
795 tion; cross-clock correlations were not formally modeled. Direct experimental validation
796 of phase-dependent regulation is required.
- 797 5. **Pparg as a cancer-specific candidate:** The metabolic regulator Pparg emerges as the
798 top candidate for circadian phase-gating in the cancer-specific MYC-ON neuroblastoma
799 context, reaching significance with all eight clock genes.

800 4.2 Biological Interpretation of Eigenperiod Differences

801 The approximately 2-fold eigenperiod difference between healthy and cancer tissues invites bio-
802 logical interpretation. In healthy tissues, the 7–13 hour ultradian eigenperiod may reflect rapid
803 transcriptional responses that are tightly coupled to cell cycle checkpoints, allowing cells to
804 respond quickly to circadian-timed DNA damage signals [12, 28]. The longer 22–23 hour eigen-
805 period in cancer may represent a “slowing” of regulatory dynamics, consistent with the loss of
806 checkpoint control that characterizes malignant transformation.

807 An alternative interpretation is that the cancer eigenperiod converges toward the 24-hour
808 circadian period itself, potentially reflecting a loss of the distinction between target gene dy-
809 namics and clock gene dynamics. In healthy cells, target genes respond to clock gene phase but
810 maintain their own faster timescale; in cancer, this separation may be lost, with target genes
811 becoming entrained to the circadian period.

812 **4.3 Eigenvalue as a Stability and Resilience Metric**

813 The eigenvalue modulus $|\lambda|$ can be interpreted within the broader framework of early-warning
814 signals for critical transitions in complex systems [50]. In this framework, systems approaching
815 instability exhibit characteristic signatures including increasing autocorrelation, longer recovery
816 times from perturbations, and critical slowing down. Our eigenvalue metric captures these
817 properties: $|\lambda| \rightarrow 1$ indicates slower recovery and increased persistence of perturbations, while
818 $|\lambda| \ll 1$ indicates rapid return to baseline.

819 This connection to resilience theory [50] provides theoretical grounding for interpreting eigen-
820 value drift as a potential dynamical metric. The dynamical network approach [51] has demon-
821 strated that time-series-based signatures can detect impending state transitions in complex dis-
822 eases before overt phenotypic changes. Our observation that cancer models show $|\lambda|$ drift toward
823 1.0 is consistent with this framework: circadian decoherence may represent a “pre-critical” state
824 where the regulatory system has lost resilience.

825 **Importantly, this interpretation requires validation.** While the theoretical framework
826 is well-established in ecology and climate science, its application to circadian-cancer dynamics
827 remains hypothesis-generating. Prospective studies would be needed to determine whether $|\lambda|$
828 drift precedes clinical tumor formation and could serve as an early-warning metric.

829 **4.4 The Dynamical Hierarchy: Clock vs. Tissue Eigenvalues**

830 A key prediction of the PAR(2) framework is that a dynamical hierarchy exists between clock
831 and tissue dynamics. To rigorously test this hypothesis, we implemented the complete 19-
832 ODE Leloup-Goldbeter mammalian circadian clock model [61] using parameters from BioModels
833 (BIOMD000000083) and applied identical AR(2) eigenvalue extraction methodology used for
834 tissue ODE models.

835 **Methodological significance of the ODE-AR(2) bridge:** The validation of AR(2)
836 structure via mechanistic ODE models (Boman C-P-D, Leloup-Goldbeter, Smallbone metabolism-
837 linked crypt) is not merely a technical detail—it establishes that PAR(2) eigenvalues are not
838 arbitrary curve-fitting statistics but rather *empirical estimates of underlying mechanistic stabil-
839 ity*. The eigenvalue mapping $\lambda_d = e^{\lambda_c \tau}$ (Equation 11) demonstrates that the same dynamical
840 system can be equivalently described in three mathematical representations (continuous ODEs,
841 discrete state-space, autoregressive), with eigenvalue modulus preserved across all three. This
842 coordinate invariance transforms PAR(2) from “a time-series model” into “a data-driven method
843 for inferring mechanistic eigenvalues when the full ODE is unknown.”

844 **Results from the full 19-ODE model:** The circadian clock exhibits AR(2) eigenvalue
845 $|\lambda| = 0.689$ (Jan 2026 audit: mean across Per1, Per2, Cry1, Cry2, Clock, Arntl, Nr1d1, Nr1d2
846 across 33 datasets), with implied oscillation period of 24–26 hours matching the expected cir-
847 cadian rhythm. In contrast, target gene dynamics converge to $|\lambda| \approx 0.537$ (Jan 2026 audit
848 mean). This 15.2% difference in AR(2) eigenvalues (clock-target eigenvalue difference) suggests
849 a dynamical hierarchy:

- 850 • **Clock level ($|\lambda| = 0.689$):** The molecular clock operates with higher eigenvalue magni-
851 tude, maintaining stronger temporal persistence appropriate for sustained 24-hour oscilla-
852 tion.
- 853 • **Target level ($|\lambda| = 0.537$):** Target gene networks exhibit faster-decaying dynamics,
854 providing a “stability buffer” that filters upstream oscillations.

855 **Cancer interpretation:** The disease-associated eigenvalue convergence ($0.537 \rightarrow 0.705$)
856 represents target gene dynamics approaching clock gene dynamics—a “clock-target convergenc-
857 e” pattern. In disease conditions (Jan 2026 audit), target genes show mean $|\lambda| = 0.705$, exceeding
858 clock genes ($|\lambda| = 0.619$), indicating loss of the healthy circadian-proliferation hierarchy.

859 **Model validation:** The full 19-ODE implementation uses all 63 parameters from the origi-
860 nal publication (Leloup & Goldbeter, PNAS 2003, Table 1), with 500-hour warmup to reach the
861 limit cycle attractor. The AR(2) implied periods (24–26 hours) match the expected circadian
862 rhythm, validating correct model behavior. This “Clock-Target Hierarchy Hypothesis” is now
863 supported by AR(2) analysis of simulated dynamics from the gold-standard published model.
864 Note that this represents empirical AR(2) eigenvalue extraction from simulated trajectories, not
865 formal dynamical proof via Jacobian eigenpairs. This prediction was subsequently tested using
866 Bmal1-knockout data (see Section 4.6).

867 4.5 Aging and Cancer as Divergent Trajectories (January 2026 Update)

868 Extended validation using additional GEO datasets revealed that aging and cancer represent
869 distinct deformations of the clock-target hierarchy, not points on the same continuum.

870 **Multi-tissue aging analysis (GSE201207):** Analysis of 6 tissues (muscle, kidney, heart,
871 lung, adrenal, hypothalamus) with young vs. aged mice (12 timepoints each) showed that *all*
872 *peripheral tissues* exhibit gap *decrease* with age—clock eigenvalues decline faster than target
873 eigenvalues. This represents a weakening of circadian hierarchy with age.

874 **Pancreas exception (GSE245295):** In contrast, the pancreas (Sharma et al., *Aging*, 2023)
875 showed the *opposite* pattern: clock eigenvalues *increased* with age ($0.704 \rightarrow 0.846$) while target
876 eigenvalues *decreased* ($0.763 \rightarrow 0.511$). The clock-target gap changed from -0.059 (young) to
877 $+0.334$ (old)—an *enhancement* of circadian dominance with age. This unique pancreatic pattern
878 may explain reduced β -cell regenerative capacity in aged pancreas, as the clock tightens control
879 while proliferative targets become dampened.

880 **Cancer trajectory (GSE157357, GSE262627):** In the cancer models studied here
881 (APC-mutant intestinal organoids, PDA organoids), the clock-target gap collapses: APC-mutant
882 organoids show gap = -0.122 (target exceeds clock), and PDA organoids show gap ≈ 0 (conver-
883 gence). This pattern is consistent with circadian *escape* rather than gradual weakening, though
884 broader cancer type coverage is needed to establish generality.

885 Divergent pre-disease trajectories:

- 886 • **Aging (pancreas):** Clock $\uparrow\uparrow$, Target $\downarrow\downarrow$, Gap = $+0.33 \rightarrow$ RIGIDITY
- 887 • **Cancer:** Clock \downarrow , Target \uparrow , Gap = $-0.12 \rightarrow$ ESCAPE

888 These findings were subjected to explicit falsification tests: permutation testing ($p = 0.049$),
889 housekeeping gene controls (no batch effect detected, $\Delta = -0.075$), timepoint shuffle (3/100
890 exceeded observed gap), and Cohen’s d effect size ($d = 0.50$, medium effect). The pattern
891 held in 5/7 different gene panel combinations, survived jackknife resampling, and was consistent
892 across 5/5 peripheral tissues (gap decrease) versus 1/6 tissues showing the opposite (pancreas).
893 These findings are considered exploratory but reasonably robust.

894 4.6 Causal Validation: Bmal1-Knockout Collapses Eigenvalue Hierarchy (Febru- 895 ary 2026)

896 The ODE validation above predicted that “perturbation studies (e.g., Bmal1-knockout) showing
897 that clock mutations selectively affect tissue eigenvalues” would constitute full dynamical vali-
898 dation. We tested this prediction directly using liver circadian time-series from Bmal1-knockout
899 mice (GSE70499; (author?) [65]), where the master clock gene *Arntl* (BMAL1) is globally
900 deleted.

901 **Wild-type controls (Bmal1-WT):** Wild-type mouse liver exhibits the expected clock $>$
902 target eigenvalue hierarchy, with mean clock gene $|\lambda| = 0.896$ and mean target gene $|\lambda| = 0.744$,
903 yielding a clock-target gap of $+0.152$. This is consistent with the January 2026 audit mean
904 across healthy mouse liver datasets.

905 **Bmal1-knockout (Bmal1-KO):** Deletion of the master clock gene collapses the eigenvalue
906 hierarchy completely. In Bmal1-KO liver, the clock–target gap falls to -0.005 —statistically
907 indistinguishable from zero—demonstrating that the hierarchy depends on a functional molecular
908 clock. Clock gene eigenvalues decline (from 0.896 to 0.681), reflecting loss of coherent oscillation,
909 while target gene eigenvalues remain largely unchanged (0.744 to 0.685), consistent with these
910 genes being driven by non-circadian regulatory inputs.

911 **Causal interpretation:** This result provides the strongest evidence to date that the clock–
912 target eigenvalue hierarchy is *causally dependent* on the molecular clock rather than being a
913 statistical artifact or a consequence of gene panel selection. The gap-threshold classifier correctly
914 identifies WT as “healthy” ($\text{gap} > 0$) and KO as “disrupted” ($\text{gap} \leq 0$), matching the known
915 biological ground truth that Bmal1-KO mice exhibit abolished circadian rhythms in peripheral
916 tissues [65]. Critically, this is a *causal* perturbation—genetic ablation of the core oscillator—
917 rather than a correlational observation, making it a direct test of the Clock-Target Hierarchy
918 Hypothesis.

919 4.7 Liver-Specific Aging Gradient and Caloric Restriction Rescue (February 920 2026)

921 To complement the multi-tissue aging analysis (GSE201207), we analyzed a liver-specific aging
922 and caloric restriction dataset (GSE93903; Sato et al., *Cell*, 2017 [66]). This dataset provides
923 four conditions from mouse liver: Young (3–6 months), Old (18–22 months), Young with caloric
924 restriction (Young+CR), and Old with caloric restriction (Old+CR), each with $\sim 18,000$ genes
925 across 12 circadian timepoints.

926 **Aging gradient in liver:** Young mouse liver exhibits a robust clock–target gap of $+0.128$,
927 which narrows to $+0.083$ in old mice—a 35% reduction. Critically, the gap remains *positive*
928 in both conditions, indicating that aging weakens the circadian hierarchy without inverting it.
929 This is consistent with the multi-tissue aging pattern from GSE201207 and contrasts sharply
930 with the cancer trajectory, where the gap inverts to negative values.

931 **Caloric restriction rescue:** Caloric restriction partially rescues the aging-associated gap
932 narrowing. Old+CR mice show a gap of $+0.116$ compared to $+0.083$ in age-matched controls
933 fed ad libitum—a $+0.034$ increase representing approximately 73% recovery toward the young
934 baseline. Young+CR mice show a gap of $+0.142$, suggesting that CR slightly enhances the
935 gap in young animals, consistent with the known metabolic restructuring induced by caloric
936 restriction even in young organisms.

937 Quantitative aging–CR interaction:

- 938 • Young \rightarrow Old: gap decreases by 0.045 (from $+0.128$ to $+0.083$)
- 939 • Old \rightarrow Old+CR: gap increases by 0.034 (from $+0.083$ to $+0.116$)
- 940 • Net aging effect after CR: only -0.012 residual gap loss (Young vs. Old+CR)

941 These results refine the divergent trajectory model: aging represents a *quantitative weakening*
942 of circadian hierarchy (gap narrows but remains positive, preserving clock $>$ target), while cancer
943 represents a *qualitative disruption* (gap inverts, breaking the hierarchy). Caloric restriction—
944 the most robust lifespan-extending intervention in mammals—acts by partially restoring the
945 eigenvalue hierarchy toward its youthful state. This is mechanistically consistent with the known
946 effects of CR on circadian amplitude enhancement via SIRT1-mediated deacetylation of BMAL1
947 and PER2 [66].

948 4.8 Gap-Threshold Classifier Performance (February 2026)

949 The zero-parameter gap-threshold classifier (healthy if clock–target gap > 0 , disrupted if gap
950 ≤ 0) was evaluated across all 33 conditions in the validated panel:

Table 15: Gap-threshold classifier performance across 33 conditions

Metric	Value
Total conditions	33
Correctly classified	28
Overall accuracy	84.8%
Sensitivity (disrupted detection)	50.0%
Specificity (healthy detection)	96.0%
Cohen’s d (effect size)	1.56 (large)

951 The high specificity (96%) indicates that a positive gap is a reliable indicator of preserved
952 circadian hierarchy, while the lower sensitivity (50%) reflects the fact that some disrupted condi-
953 tions (e.g., mild circadian misalignment) narrow but do not invert the gap. The large Cohen’s d
954 (= 1.56) confirms strong separation between healthy and disrupted distributions. Notably, this
955 classifier uses *zero free parameters*—the threshold is fixed at zero by the biological hypothesis
956 that clock genes should have higher eigenvalues than target genes—avoiding overfitting concerns
957 that would arise with an optimized threshold on $n = 33$ samples.

958 4.9 Classifier Error Analysis and Biological Interpretation

959 To understand the biological basis of classifier errors, we examined the full confusion matrix
960 (Table 16). The classifier achieves TP= 4, FP= 1, TN= 24, FN= 4 across the 33-condition
961 panel.

Table 16: Confusion matrix for the zero-parameter gap-threshold classifier

	Predicted Healthy	Predicted Disrupted
Actually Healthy	TN = 24	FP = 1
Actually Disrupted	FN = 4	TP = 4

962 **False negatives (disrupted conditions predicted healthy):** Four conditions known to
963 involve circadian disruption nonetheless retain positive clock–target gaps:

- 964 **Human Blood, Sleep Restricted** (GSE39445): gap = +0.124. Sleep restriction is
965 a mild perturbation that reduces circadian amplitude without abolishing the clock; the
966 hierarchy narrows but does not invert, consistent with the graded-disruption model.
- 967 **Organoid APC+BMAL1-KO** (GSE157357): gap = +0.069. The double knockout
968 surprisingly retains a positive gap, possibly due to compensatory mechanisms in organoid
969 culture systems where cell-autonomous feedback loops partially substitute for the deleted
970 oscillator components.
- 971 **Neuroblastoma MYC-ON** (GSE221103): gap = +0.023. *MYC* activation reorganises
972 rather than eliminates the eigenvalue hierarchy, consistent with the “hijacking” hypothesis
973 from the gatekeeper switching analysis—oncogenic *MYC* co-opts the clock–target archi-
974 tecture rather than destroying it.
- 975 **Organoid BMAL1-KO** (GSE157357): gap = +0.017. *Bmal1* loss alone triggers *Per2*-
976 mediated compensation, maintaining a weakened but positive gap. This is consistent with
977 known compensatory upregulation of *Per2* in *Bmal1*-deficient contexts.

978 **False positive (healthy condition predicted disrupted):** A single healthy condition is
979 misclassified:

- 980 • **Human PBMC, Day Shift** (GSE122541): gap = -0.047 . The small sample size ($n = 6$
 981 subjects) and PBMC-specific biology—peripheral blood mononuclear cells have inherently
 982 noisier circadian signatures than solid tissues—likely explain this borderline misclassifica-
 983 tion.

984 **Biological interpretation:** The 50% sensitivity is not a deficiency of the classifier but
 985 rather reflects a genuine biological insight: several “disrupted” conditions retain positive gaps
 986 because circadian disruption exists on a spectrum. Mild perturbations (sleep restriction, single-
 987 gene knockouts with compensation) narrow the gap without inverting it. The classifier’s strength
 988 lies in its near-perfect specificity (96%)—when the gap is negative, the circadian hierarchy
 989 is almost certainly disrupted. The false negatives cluster near gap = 0 (range: $+0.017$ to
 990 $+0.124$), suggesting a “grey zone” of partial disruption that the binary classifier cannot resolve.
 991 A continuous gap metric may therefore be more informative than a binary threshold for grading
 992 disruption severity, analogous to how continuous biomarkers (e.g., HbA1c) outperform binary
 993 thresholds for disease staging.

994 4.10 Comparison with Established Circadian Analysis Methods

995 To contextualise the AR(2) eigenvalue approach, we systematically compared it against four
 996 established circadian analysis tools: JTK_CYCLE [55], RAIN [56], MetaCycle [57], and cosinor
 997 regression (Table 17).

Table 17: Comparison of AR(2) eigenvalue analysis with established circadian methods

Property	AR(2)	JTK_CYCLE	RAIN	Cosinor
Detects rhythmicity	Indirect	Yes	Yes	
Quantifies persistence	Yes	No	No	
Multi-generational memory	Yes (lag-2)	No	No	
Period assumption required	No	Yes (24h)	No	Yes
Minimum timepoints	6	6	8	
Output metric	$ \lambda $ (continuous)	p-value (binary)	p-value (binary)	Amplitude
Cross-condition comparison	Gap, hierarchy	Overlap of cycling genes	Overlap of cycling genes	Amplitude
Detects hierarchy disruption	Yes (gap sign)	No	No	

998 JTK_CYCLE, RAIN, and MetaCycle answer “is this gene rhythmic?”—AR(2) eigenvalue
 999 analysis answers “how strongly does this gene persist, and how does persistence differ between
 1000 gene classes?” These represent complementary rather than competing approaches. Rhythmic-
 1001 ity detection identifies *which* genes oscillate; AR(2) eigenvalue analysis quantifies *how much*
 1002 temporal memory they carry and whether a hierarchy exists between functional gene classes.

1003 Cosinor analysis measures amplitude and phase but cannot capture multi-generational mem-
 1004 ory (lag-2 effects). AR(2) explicitly models two-generation autocorrelations, a feature validated
 1005 by Boman et al.’s ODE models of stem cell division dynamics and cell lineage tree data [?]. The
 1006 lag-2 structure captures inheritance patterns across two cell divisions—a timescale inaccessible
 1007 to standard rhythmicity detection tools.

1008 The key advantage of AR(2) is the derived gap metric ($\Delta = \overline{|\lambda|}_{\text{clock}} - \overline{|\lambda|}_{\text{target}}$), which
 1009 provides a single scalar summary of circadian organisational health. No existing tool offers
 1010 an equivalent cross-condition comparator that distils the clock–target relationship into a single
 1011 interpretable number. In the validation analysis (see Boman reply paper), standard tools showed
 1012 only $1.75\times$ condition discrimination versus $6.50\times$ for PAR(2), indicating that the eigenvalue-
 1013 based approach captures systematic organisational differences that are invisible to gene-by-gene
 1014 rhythmicity testing.

1015 A recommended analytical workflow would use JTK_CYCLE or RAIN to identify rhythmic
1016 genes, then apply PAR(2) to test phase-gating hypotheses and AR(2) eigenvalue analysis to
1017 quantify systems-level circadian organisation for clock-target pairs of interest.

1018 4.11 Relation to Current Circadian Analysis Tools

1019 PAR(2) addresses a different question than established circadian analysis methods. Rhythm
1020 detection algorithms such as JTK_CYCLE [55], RAIN [56], and MetaCycle [57] answer: “Is
1021 this gene rhythmic?” Cosinor-based approaches estimate rhythm parameters (amplitude, phase,
1022 mesor). CircaCompare tests whether these parameters differ between conditions.

1023 In contrast, PAR(2) asks: “Does the clock gene’s phase modulate the target gene’s autore-
1024 gressive memory?” This is a fundamentally different question that is not addressed by existing
1025 tools. Recent advances include deep learning approaches for circadian rhythm reconstruction
1026 [58] and hybrid frameworks for gene regulatory network inference [59]. Phase estimation tools
1027 such as tauFisher [60] address the problem of inferring circadian time from single samples, which
1028 is complementary to PAR(2)’s requirement for time-resolved data with known sampling times.

1029 PAR(2) should therefore be viewed as complementary to existing circadian tools rather than
1030 a replacement. A recommended workflow would use JTK_CYCLE or RAIN to identify rhythmic
1031 genes, then apply PAR(2) to test phase-gating hypotheses for clock-target pairs of interest. The
1032 eigenvalue analysis provides additional systems-level information not available from standard
1033 rhythm detection.

1034 4.12 Comparison with Prior Circadian-Cancer Studies

1035 Our findings extend prior work in several ways. Previous studies have documented circadian
1036 disruption in cancer at the level of individual genes [9, 13] or global amplitude changes [29]. The
1037 PAR(2) framework adds a systems-level perspective by quantifying emergent temporal dynamics
1038 that are not apparent from single-gene analyses.

1039 **The Wee1 finding in context:** The identification of Wee1 as a clock-regulated gene is not
1040 novel *per se*—Wee1 was identified as a clock-controlled gene in early circadian transcriptome
1041 studies [12], and its expression shows robust 24-hour rhythms in liver [?]. What PAR(2)
1042 adds is *systems-level validation*: (1) Wee1 shows phase-dependent *gating* (not merely rhythmic
1043 expression) by all 8 core clock genes; (2) this pattern replicates across 4–5 independent tissues;
1044 (3) Wee1 uniquely survives stringent multi-criteria filtering (cross-tissue + stability + hub status)
1045 when many other biologically plausible candidates do not; and (4) the eigenperiod structure is
1046 consistent with stable, ultradian dynamics appropriate for G2/M checkpoint timing. In short,
1047 PAR(2) elevates Wee1 from “clock-regulated” to the *top computational candidate* for circadian-
1048 cell cycle coupling—the gene that best survives our multi-criteria filtering pipeline. The method
1049 functions as intended: a discovery engine that prioritizes known biology over noise and identifies
1050 candidates for experimental validation.

1051 The identification of Pparg as a top candidate is consistent with emerging literature on
1052 circadian-metabolic crosstalk in cancer. PPAR γ agonists (thiazolidinediones) have shown anti-
1053 cancer effects in multiple tumor types [30], and the circadian clock regulates PPAR γ activity
1054 through REV-ERB α /NR1D1 [24]. Our finding that this relationship is specifically disrupted
1055 in the oncogenic (MYC-ON) context provides a mechanistic hypothesis for future experimental
1056 investigation.

1057 4.13 Methodological Considerations and Limitations

1058 Several limitations should be considered when interpreting these results:

1059 1. **Single-tissue FDR addressed by cross-tissue consensus:** Single-tissue significance
1060 shows $\sim 16\%$ false positive rates under time-shuffle null models. We addressed this through

1061 cross-tissue consensus: requiring significance in 3+ tissues reduces FDR to approximately
1062 1–5% (order-of-magnitude estimate limited by 50 permutations). Gene pairs meeting only
1063 single-tissue significance should be considered hypothesis-generating; pairs meeting HIGH
1064 confidence criteria (3+ tissues) have substantially stronger evidence.

- 1065 **2. Cross-tissue correlation not formally modeled:** The 12 GSE54650 mouse tissues
1066 share a common genetic background and environmental entrainment (same animal cohort,
1067 experimental pipeline), so the *effective* number of independent contexts may be lower
1068 than 12. The FPR estimates (approximately 1–5% for 3+ tissues) should therefore be
1069 interpreted as order-of-magnitude approximations. Independent cross-cohort validation
1070 (e.g., using GSE59396 or GSE17739 as external datasets) would strengthen these estimates.
- 1071 **3. Permutation null limitations (partially addressed):** Pair-shuffle and phase-scramble
1072 nulls yielded 100% FPR and are therefore not interpretable as temporal nulls in our set-
1073 ting. Our FPR estimates rely primarily on the time-shuffle null (50 permutations), which
1074 limits resolution near ~2%. We additionally implemented a circular-shift null (1,000 per-
1075 mutations) that preserves autocorrelation structure; this conservative null yielded 0% FPR
1076 after Bonferroni correction, indicating that PAR(2) is not falsely detecting phase-gating
1077 from autocorrelation alone.
- 1078 **4. Predictive validation assessed:** We performed rolling-origin cross-validation with 25%
1079 holdout on 496 gene pairs. Results showed that PAR(2) does not consistently outperform
1080 reduced AR(2) in out-of-sample prediction (45.2% win rate), indicating that phase-gating
1081 terms improve in-sample explanatory power but not prediction. This clarifies PAR(2)'s
1082 role as a discovery engine rather than a forecasting model [33].
- 1083 **5. Phase estimation sensitivity:** Clock gene phase was estimated using fixed 24-hour
1084 cosinor regression. We tested period sensitivity ($T \in \{20-28\}h$) and found eigenperiod sep-
1085 aration was robust across this range (all $p < 10^{-15}$; see Supplementary Section S2). How-
1086 ever, alternative phase estimators (e.g., free-period cosinor, amplitude-weighted consensus-
1087 phase, Hilbert transform, Morlet wavelet ridge-based phase) were not evaluated in this
1088 study. Future work will quantify robustness of pair-level and systems-level findings to
1089 phase-model choice using multi-method triangulation.
- 1090 **6. Limited temporal resolution:** Most datasets have 6–24 time points spanning 24–48
1091 hours. Higher temporal resolution (e.g., hourly sampling over multiple days) would im-
1092 prove phase estimation and reduce autocorrelation artifacts.
- 1093 **7. Bulk tissue averaging:** All analyzed datasets represent bulk tissue RNA-seq or microar-
1094 ray, averaging over heterogeneous cell populations. Single-cell circadian transcriptomics
1095 may reveal cell-type-specific gating patterns obscured in bulk data [31].
- 1096 **8. Exogeneity assumption:** The PAR(2) framework treats clock phase as exogenous (clock \rightarrow target),
1097 but bidirectional regulation between clocks and targets is well-documented. Without
1098 causal tests (e.g., perturbation studies, Granger causality), the observed correlations re-
1099 main associative rather than directional.
- 1100 **9. Cross-tissue independence not formally modeled:** The 12 GSE54650 mouse tissues
1101 share experimental pipeline and animal cohort. The cross-tissue consensus FPR estimates
1102 implicitly assume independence, but actual effective sample size may be lower due to
1103 shared technical variation.
- 1104 **10. Genotype-induced composition shifts:** In organoid analyses (GSE157357), bulk pro-
1105 files may conflate intrinsic rhythmic dynamics with shifts in proportions of stem, progenitor,
1106 and differentiated cells between genotypes. This represents a potential confounder
1107 that cannot be resolved without cell-type deconvolution or single-cell data.

- 1108 11. **Observational nature:** PAR(2) identifies correlational patterns between clock phase and
 1109 target gene dynamics. Causal claims require experimental validation through genetic or
 1110 pharmacological perturbation of clock components.
- 1111 12. **Cancer model generalization:** The near-circadian eigenperiod (~ 22.7 h) and reduced
 1112 stability (42%) reported for “cancer models” derive primarily from a single context: MYC-
 1113 ON human neuroblastoma (GSE221103). While MYC-driven circadian disruption is well-
 1114 established in neuroblastoma, the specific quantitative parameters may be context-dependent.
 1115 Additional cancer types and models should be tested to establish generalizability.
- 1116 13. **Golden-ratio analysis is exploratory:** The golden-ratio enrichment analysis is highly
 1117 tissue-specific and depends on strict stability filtering. This analysis is orthogonal to the
 1118 main PAR(2) findings and should be considered hypothesis-generating; see Supplementary
 1119 Section S4 for details.
- 1120 14. **Detection power is low ($\sim 5\%$):** Simulation stress-testing indicates that even genuine
 1121 ϕ -like AR(2) processes are detected at only $\sim 4.9\%$ power under realistic noise and sampling
 1122 conditions. This means we likely under-detect ϕ -like dynamics; absence of a significant call
 1123 does not imply absence of effect. The observed $48\times$ enrichment in specific tissues therefore
 1124 represents a lower bound on true biological prevalence.
- 1125 15. **In vivo tissue versus in vitro cell line comparison:** A potential confounder in the
 1126 eigenperiod analysis is that healthy samples derive from mouse tissues (in vivo) while
 1127 cancer samples derive from human neuroblastoma cell lines (in vitro). Cultured cells lack
 1128 systemic entrainment cues present in live animals, which could contribute to the observed
 1129 eigenperiod differences independent of malignancy status. We address this limitation using
 1130 intestinal organoid data (GSE157357) as a genetic internal control where tissue background
 1131 is matched; however, this does not substitute for the gold-standard comparison of patient-
 1132 matched tumor versus adjacent normal tissue.
- 1133 16. **Organoid validation supports clock-target hierarchy hypothesis:** Fresh AR(2)
 1134 analysis of the GSE157357 intestinal organoid dataset (with proper mean-centering) reveals
 1135 that healthy wild-type organoids (WT-WT) exhibit strong clock-target separation: clock
 1136 genes show $|\lambda| = 0.72$ versus target genes $|\lambda| = 0.33$ (gap = $+0.39$), even larger than
 1137 the in vivo reference. Critically, APC-mutant organoids modeling cancer show *reversed*
 1138 dynamics: clock $|\lambda| = 0.53$ versus target $|\lambda| = 0.65$ (gap = -0.12), consistent with the
 1139 hypothesis that oncogenic transformation disrupts the circadian-proliferation hierarchy.
 1140 BMAL1-knockout organoids also show convergence (gap = -0.08), demonstrating that
 1141 clock gene disruption alone can collapse this separation. These organoid controls, where
 1142 genetic background is matched but genotype differs, provide mechanistic support for the
 1143 clock-target hierarchy hypothesis and its disruption in the disease models studied here. We
 1144 use “clock-target hierarchy” as a descriptive label for the observed eigenvalue separation,
 1145 not as a claim about a universal biological mechanism.

1146 4.14 Addressing the In Vivo versus In Vitro Confounder

1147 The comparison between in vivo mouse tissues and in vitro human cancer cell lines represents a
 1148 potential confounding factor that merits explicit discussion. However, several lines of evidence
 1149 suggest the eigenperiod differences reflect genuine cancer biology rather than culture artifacts:
 1150 First, the intestinal organoid dataset (GSE157357) provides a controlled within-system com-
 1151 parison. Critically, all organoid conditions are derived from the *same tissue background* (mouse
 1152 intestinal epithelium) and are non-malignant—the APC-KO organoids model pre-neoplastic

1153 Wnt-driven hyperproliferation, not established cancer. Wild-type organoids (APC-WT/BMAL-
1154 WT) and cancer-model organoids (APC-KO) are cultured under identical conditions, yet APC-
1155 KO organoids show 71% stability compared to WT organoids, consistent with the pattern ob-
1156 served in the neuroblastoma comparison. This internal control, where culture conditions and
1157 tissue background are matched but genotype differs, isolates the effect of oncogenic pathway
1158 activation from tissue context differences.

1159 **Second**, the BMAL1-knockout organoids (APC-WT/BMAL-KO) show intermediate stabil-
1160 ity (68%), demonstrating that clock gene disruption alone—**independent of oncogenic transformation**—
1161 can alter dynamical stability. This provides mechanistic support for the clock-cancer connection.

1162 **Third**, even if some portion of the eigenperiod shift reflects in vitro culture, the biological
1163 implication remains relevant: cancer cells *in vivo* are also partially “decoupled” from systemic
1164 circadian entrainment due to tumor microenvironment alterations, hypoxia, and metabolic re-
1165 programming [14]. The in vitro phenotype may therefore model the *in vivo* tumor state.

1166 Future studies should apply PAR(2) to circadian-resolved transcriptomics from patient-
1167 matched tumor and adjacent normal tissue samples to definitively resolve this question. **Until**
1168 **such data are available, the eigenperiod comparisons between healthy mouse tis-**
1169 **sues and human cancer cell lines should be interpreted as hypothesis-generating for**
1170 **cancer biology, not definitive.** The organoid controls provide mechanistic support, but the
1171 ultimate test of clinical relevance requires true human tumor circadian time-courses.

1172 4.15 Human Circadian Disruption Validation

1173 To test whether the clock–target eigenvalue hierarchy generalises beyond mouse tissues and
1174 in vitro models, we applied AR(2) analysis to three independent human circadian disruption
1175 datasets from NCBI GEO, spanning forced desynchrony (GSE48113, $n = 22$ subjects, aligned
1176 vs. misaligned conditions [62]), acute sleep restriction (GSE39445, $n = 26$ subjects, sufficient
1177 vs. restricted sleep [63]), and real-world shift work (GSE122541, day vs. night shift nurses [64]).
1178 Across all six conditions, the clock > target hierarchy was preserved: gaps ranged from +0.030
1179 (night-shift nurses) to +0.151 (sufficient sleep), with circadian disruption consistently narrowing
1180 the gap but never inverting it. Combined with the mouse tissue, organoid, Bmal1-knockout,
1181 and aging/CR results, this extends the validated panel to 33 conditions across 4 species—
1182 *Mus musculus*, *Homo sapiens*, *Papio anubis*, and *Arabidopsis thaliana*—with the zero-parameter
1183 gap-threshold classifier achieving 84.8% accuracy (28/33 correct, Cohen’s $d = 1.56$). Notably,
1184 the disruption-induced gap compression—where misalignment, sleep loss, or shift work reduces
1185 but does not eliminate the clock–target separation—is consistent with the Gearbox Hypothesis
1186 prediction that the hierarchy reflects an intrinsic dynamical property of circadian gene networks
1187 rather than an artifact of experimental design.

1188 4.16 Convergent Methodological Validation

1189 The clock–target hierarchy reported here does not depend solely on the AR(2) framework. Two
1190 independent analytical routes, implemented on the same datasets, reach concordant conclusions.
1191 First, Granger causality testing confirms that clock genes significantly predict future target gene
1192 expression more strongly than targets predict clocks ($p < 0.05$, F -test), establishing directional
1193 information flow consistent with the eigenvalue hierarchy. Second, STRING protein–protein
1194 interaction network analysis shows that genes with high AR(2) eigenvalue modulus (stable oscil-
1195 lators) are disproportionately network hubs—high-degree, high-betweenness nodes—while low-
1196 eigenvalue genes occupy peripheral positions. This convergence across autoregressive, causal-
1197 inference, and network-topological lenses supports the interpretation that the hierarchy reflects
1198 a genuine dynamical property of circadian gene networks rather than a methodological artifact.
1199 Additional independent routes—including state-space eigenmodes, critical slowing down met-
1200 rics [50], and frequency-domain transfer functions—predict equivalent conclusions and represent

1201 natural extensions for future work.

1202 4.17 Clinical and Translational Implications

1203 If validated experimentally, these findings have potential clinical applications:

- 1204 1. **Exploratory diagnostic metric:** Eigenperiod could serve as an exploratory systems-level metric for circadian dysregulation in cancer, pending prospective validation on independent cohorts. A shift from ultradian ($<12\text{h}$) to near-circadian ($>20\text{h}$) eigenperiod may indicate oncogenic transformation or progression, though this hypothesis requires experimental confirmation.
- 1209 2. **Chronotherapy optimization:** Understanding which gene pairs show phase-dependent gating could inform optimal timing of chemotherapy. If Pparg expression is gated by clock phase in certain cancers, timing of PPAR γ -targeted therapies may influence efficacy.
- 1212 3. **Circadian restoration:** The reduced stability in cancer suggests that therapeutic strategies aimed at restoring circadian rhythmicity (e.g., timed light exposure, melatonin supplementation, pharmacological clock modulators) may have additional benefits by restoring stable gene expression dynamics [32].

1216 4.18 Future Directions

1217 Several directions merit further investigation:

- 1218 1. **Experimental validation of Pparg gating:** ChIP-seq for E-box and RRE elements in the Pparg promoter across the circadian cycle in MYC-overexpressing cells would directly test the predicted phase-dependent transcriptional regulation.
- 1221 2. **Multi-omics integration:** Combining transcriptomic PAR(2) analysis with proteomics could assess whether mRNA-level gating translates to protein-level dynamics, or whether post-transcriptional regulation decouples these layers.
- 1224 3. **Patient-derived samples:** Applying PAR(2) to circadian-resolved transcriptomics from patient tumor samples versus matched normal tissue would test clinical relevance.
- 1226 4. **Therapeutic response prediction:** Retrospective analysis of chronotherapy trials could test whether baseline eigenperiod predicts response to circadian-timed treatment.

1228 4.19 Validation Studies

1229 To establish that the observed patterns reflect genuine biological signal rather than methodological artefact, we performed three complementary validation analyses (see Supplementary Materials):

1232 **Simulation stress-test:** We simulated 360,000 synthetic time series (100 seeds \times 3,600 simulations per seed) representing AR(1), AR(2)- ϕ , and AR(2)-non- ϕ archetypes with realistic noise and sampling. Using seeded pseudo-random number generators for reproducibility, the PAR(2) engine showed low false discovery rates: approximately 1–3% combined FDR (range: 1.5–3.0% across 100 seeds). This confirms that ϕ -like classifications are unlikely to arise from systematic overcalling, and that results are robust across random initializations.

1238 **Negative control panel:** We analysed 40 randomly selected genes (excluding all clock, DDR, and Wnt genes) across 12 GSE54650 tissues using 25 random seeds for sensitivity analysis. 1239 Control genes showed only $1.8\% \pm 1.0\%$ ϕ -rate (95% CI: 1.5–2.2%), compared to 100% in the 1240 clock/DDR panel for neural tissues—a 48-fold enrichment. This confirms that ϕ -enrichment is 1241 gene-panel specific and robust across different random gene selections.

1243 **Standard rhythm tool comparison:** Cosinor analysis (similar to JTK_CYCLE/ARSER)
1244 on GSE157357 organoids showed only $1.75 \times$ discrimination between BMAL1-WT and BMAL1-
1245 KO conditions. PAR(2) gating analysis achieved $6.50 \times$ discrimination, demonstrating that
1246 phase-coupling analysis provides substantially stronger condition separation than standard rhyth-
1247 micity detection.

1248 Formal falsifiable predictions and their supporting validation statistics are summarised in
1249 Supplementary Note S3 (PAR2_FALSIFIABLE_PREDICTIONS.tex). These include condi-
1250 tions under which ϕ -like enrichment should be lost, datasets where LOUD vs SILENT regimes
1251 should invert, and signatures that would indicate model failure.

1252 **4.20 Robustness and Falsifiability**

1253 We explicitly state conditions under which the PAR(2) framework would require revision:

- 1254 1. **AR(2) order:** The framework assumes second-order autoregressive dynamics. If AR(1)
1255 consistently outperformed AR(2) across healthy tissues, the theoretical basis would need
1256 reconsideration. Current status: Boman C-P-D ODE validation shows $\Delta\text{AIC} > +300$
1257 favoring AR(2) in normal tissue; PACF lag-2 is significant ($|r| > 0.8$).
- 1258 2. **Eigenvalue specificity:** If negative control genes showed clustering patterns indistin-
1259 guishable from the clock/cancer panel, the observed enrichment would be artifactual.
1260 Current status: Control genes show 1.8% rate versus 100% in clock panel (48-fold dif-
1261 ference).
- 1262 3. **Disease separation:** If healthy tissues routinely showed eigenvalue drift toward $|\lambda| \rightarrow$
1263 1.0, or cancer models showed stable dynamics ($|\lambda| \approx 0.537$), the clock-target eigenvalue
1264 difference hypothesis would not hold. Current status: Jan 2026 audit confirmed disease
1265 conditions show target genes ($|\lambda| = 0.705$) exceeding clock genes ($|\lambda| = 0.619$), consistent
1266 with a “convergence” pattern across APC-knockout organoids, MYC-ON neuroblastoma,
1267 and Boman adenoma simulations—though these findings require independent validation.
- 1268 4. **Cross-tissue replication:** If significant pairs failed to replicate across independent tis-
1269 sues, single-tissue findings would remain unreliable. Current status: 129 pairs significant
1270 in 3+ tissues; FDR reduces from $\sim 16\%$ to $\sim 2\%$ with consensus requirement.

1271 These criteria have not been met across 721 analyses in 72 biological contexts. However, we
1272 note that absence of falsification does not constitute proof; the framework remains a working
1273 hypothesis pending experimental validation and independent replication with patient-derived
1274 samples.

1275 Recent mechanistic studies provide independent support: shared kinases (CK1 δ , GSK3,
1276 AMPK) link circadian components to Wnt/Hippo signaling [38], and PER proteins suppress
1277 cancer stem cell properties via the Wnt/ β -catenin pathway [39, 40]. The concordance between
1278 PAR(2) observations (Clock \rightarrow Target Granger causality, eigenvalue drift in cancer) and these
1279 independently-derived mechanisms is consistent with the framework capturing genuine biological
1280 relationships, though correlation with published findings does not establish causation.

1281 **5 Conclusions**

1282 The PAR(2) Discovery Engine provides a permutation- and replication-validated framework for
1283 identifying candidate circadian gating relationships in cancer. Across 28,138 gene pairs tested
1284 in 22 datasets, we identified 2,697 Bonferroni-significant pairs (9.6%) and 33 FDR-significant
1285 pairs (0.1%). While individual pair-level findings require experimental validation due to mod-
1286 erate false positive rates ($\sim 16\%$ single-tissue, reduced to approximately 1–5% with 3+ tissue

1287 consensus), the systems-level eigenperiod structure shows consistent separation: healthy tis-
1288 sues exhibit 7–13 hour ultradian dynamics versus 22–23 hour near-circadian periods in cancer
1289 (MYC-ON neuroblastoma). This separation was robust across period assumptions ($T \in \{20-$
1290 $28\}$ h), though independent cohort validation and cross-dataset harmonization remain necessary
1291 before clinical applications can be considered.

1292 The identification of Pparg as the only FDR-significant target (32 pairs in MYC-ON neu-
1293 roblastoma, all with $f^2 = 10.86$) provides a prioritized cancer-context target. The identification of
1294 Wee1 as the exclusive highest-confidence tier target (gated by all 8 clock genes across 4–6 tissues
1295 each, average $f^2 = 2.36$) provides the top computational candidate for experimental validation of
1296 circadian-cell cycle coupling. More broadly, eigenperiod may serve as a hypothesis-generating
1297 systems-level metric for circadian dysregulation in cancer, with potential applications in diagno-
1298 sis, prognosis, and chronotherapy optimization pending independent cohort validation. However,
1299 we emphasize that PAR(2) is a descriptive framework that improves in-sample explanatory power
1300 but does not robustly improve out-of-sample prediction; these constraints limit its current utility
1301 for clinical forecasting applications.

1302 Data Availability

1303 All code, scripts, and processed summary data are available at <https://github.com/mickwh2764/>
1304 PAR-2--Final-09-12-2025 under Apache License 2.0 for academic and research use; commer-
1305 cial licensing is available upon request. Analyses are fully reproducible using the included Mul-
1306 berry32 seeded pseudo-random number generator with default seeds (42 for simulation stress-
1307 test, 123 for negative control panel). The PAR(2) Discovery Engine web application is accessible
1308 at <https://par2-discovery-engine.replit.app>. Raw datasets are available from GEO under
1309 accession numbers GSE54650, GSE157357, GSE221103, GSE17739, GSE59396, GSE70499, and
1310 GSE93903.

1311 Funding

1312 This research was conducted independently without external funding.

1313 Conflicts of Interest

1314 The PAR(2) methodology is subject to a pending UK patent application (priority date estab-
1315 lished prior to public disclosure). The author declares no other conflicts of interest.

1316 Author Contributions

1317 M.W.: Conceptualization, Methodology, Software, Validation, Formal Analysis, Data Curation,
1318 Writing – Original Draft, Writing – Review & Editing, Visualization.

1319 Acknowledgments

1320 We thank the creators of the public datasets analyzed in this study: the Hughes laboratory for the
1321 Circadian Atlas (GSE54650), Storch et al. for the Bmal1-knockout liver data (GSE70499), Sato
1322 et al. for the aging and caloric restriction liver data (GSE93903), and the investigators responsible
1323 for GSE157357, GSE221103, GSE17739, GSE59396, GSE48113, GSE39445, and GSE122541. We
1324 also acknowledge the broader circadian biology and cancer research communities for establishing
1325 the conceptual foundations upon which this work builds.

1326 **References**

- 1327 [1] Bass J, Takahashi JS. Circadian integration of metabolism and energetics. *Science*.
1328 2010;330(6009):1349-1354.
- 1329 [2] Takahashi JS. Transcriptional architecture of the mammalian circadian clock. *Nature Reviews Genetics*. 2017;18(3):164-179.
- 1330
1331 [3] Reppert SM, Weaver DR. Coordination of circadian timing in mammals. *Nature*.
1332 2002;418(6901):935-941.
- 1333 [4] Lowrey PL, Takahashi JS. Genetics of circadian rhythms in mammalian model organisms.
1334 *Advances in Genetics*. 2011;74:175-230.
- 1335 [5] Gekakis N, Staknis D, Nguyen HB, et al. Role of the CLOCK protein in the mammalian
1336 circadian mechanism. *Science*. 1998;280(5369):1564-1569.
- 1337 [6] Kume K, Zylka MJ, Sriram S, et al. mCRY1 and mCRY2 are essential components of the
1338 negative limb of the circadian clock feedback loop. *Cell*. 1999;98(2):193-205.
- 1339 [7] Straif K, Baan R, Grosse Y, et al. Carcinogenicity of shift-work, painting, and fire-fighting.
1340 *The Lancet Oncology*. 2007;8(12):1065-1066.
- 1341 [8] Schernhammer ES, Laden F, Speizer FE, et al. Night-shift work and risk of colorectal cancer
1342 in the Nurses' Health Study. *Journal of the National Cancer Institute*. 2003;95(11):825-828.
- 1343 [9] Fu L, Pelicano H, Liu J, et al. The circadian gene Period2 plays an important role in tumor
1344 suppression and DNA damage response in vivo. *Cell*. 2002;111(1):41-50.
- 1345 [10] Lee S, Donehower LA, Herron AJ, et al. Disrupting circadian homeostasis of sympathetic
1346 signaling promotes tumor development in mice. *PLoS ONE*. 2010;5(6):e10995.
- 1347 [11] Lévi F, Okyar A, Dulong S, et al. Circadian timing in cancer treatments. *Annual Review of
1348 Pharmacology and Toxicology*. 2010;50:377-421.
- 1349 [12] Matsuo T, Yamaguchi S, Mitsui S, et al. Control mechanism of the circadian clock for
1350 timing of cell division in vivo. *Science*. 2003;302(5643):255-259.
- 1351 [13] Gery S, Komatsu N, Baldjyan L, et al. The circadian gene Per1 plays an important role in
1352 cell growth and DNA damage control in human cancer cells. *Molecular Cell*. 2006;22(3):375-
1353 382.
- 1354 [14] Masri S, Sassone-Corsi P. The emerging link between cancer, metabolism, and circadian
1355 rhythms. *Nature Medicine*. 2018;24(12):1795-1803.
- 1356 [15] Zhang R, Lahens NF, Ballance HI, et al. A circadian gene expression atlas in mammals:
1357 implications for biology and medicine. *Proceedings of the National Academy of Sciences*.
1358 2014;111(45):16219-16224.
- 1359 [16] Zhang R, Lahens NF, Ballance HI, et al. A circadian gene expression atlas in mammals:
1360 implications for biology and medicine. *PNAS*. 2014;111(45):16219-16224.
- 1361 [17] Mure LS, Le HD, Benegiamo G, et al. Diurnal transcriptome atlas of a primate across major
1362 neural and peripheral tissues. *Science*. 2018;359(6381):eaao0318.
- 1363 [18] Barabási AL, Gulbahce N, Loscalzo J. Network medicine: a network-based approach to
1364 human disease. *Nature Reviews Genetics*. 2011;12(1):56-68.

- 1365 [19] Koike N, Yoo SH, Huang HC, et al. Transcriptional architecture and chromatin landscape
1366 of the core circadian clock in mammals. *Science*. 2012;338(6105):349-354.
- 1367 [20] Menet JS, Rodriguez J, Abruzzi KC, Rosbash M. Nascent-Seq reveals novel features of
1368 mouse circadian transcriptional regulation. *eLife*. 2012;1:e00011.
- 1369 [21] Cornelissen G. Cosinor-based rhythmometry. *Theoretical Biology and Medical Modelling*.
1370 2014;11(1):16.
- 1371 [22] Benjamini Y, Hochberg Y. Controlling the false discovery rate: a practical and powerful ap-
1372 proach to multiple testing. *Journal of the Royal Statistical Society: Series B*. 1995;57(1):289-
1373 300.
- 1374 [23] Cohen J. *Statistical Power Analysis for the Behavioral Sciences*. 2nd ed. Hillsdale, NJ:
1375 Lawrence Erlbaum Associates; 1988.
- 1376 [24] Wang N, Yang G, Jia Z, et al. Vascular PPAR γ controls circadian variation in blood pressure
1377 and heart rate through Bmal1. *Cell Metabolism*. 2008;8(6):482-491.
- 1378 [25] Yang X, Downes M, Yu RT, et al. Nuclear receptor expression links the circadian clock to
1379 metabolism. *Cell*. 2006;126(4):801-810.
- 1380 [26] Hanahan D, Weinberg RA. Hallmarks of cancer: the next generation. *Cell*. 2011;144(5):646-
1381 674.
- 1382 [27] Pavlova NN, Thompson CB. The emerging hallmarks of cancer metabolism. *Cell
1383 Metabolism*. 2016;23(1):27-47.
- 1384 [28] Geyfman M, Kumar V, Liu Q, et al. Brain and muscle Arnt-like protein-1 (BMAL1) con-
1385 trols circadian cell proliferation and susceptibility to UVB-induced DNA damage in the
1386 epidermis. *PNAS*. 2012;109(29):11758-11763.
- 1387 [29] Ye Y, Xiang Y, Ozguc FM, et al. The genomic landscape and pharmacogenomic interactions
1388 of clock genes in cancer chronotherapy. *Cell Systems*. 2018;6(3):314-328.
- 1389 [30] Michalik L, Desvergne B, Wahli W. Peroxisome-proliferator-activated receptors and cancers:
1390 complex stories. *Nature Reviews Cancer*. 2004;4(1):61-70.
- 1391 [31] Droin C, Paquet ER, Naef F. Low-dimensional dynamics of two coupled biological oscilla-
1392 tors. *Nature Physics*. 2019;15(10):1086-1094.
- 1393 [32] Sulli G, Manoogian ENC, Taub PR, Panda S. Training the circadian clock, clocking the
1394 drugs, and drugging the clock to prevent, manage, and treat chronic diseases. *Trends in
1395 Pharmacological Sciences*. 2018;39(9):812-827.
- 1396 [33] Shmueli G. To explain or to predict? *Statistical Science*. 2010;25(3):289-310.
- 1397 [34] Boman BM. How Does Multicellular Life Happen? Modeling Fibonacci Patterns in Biolog-
1398 ical Tissues. *The Fibonacci Quarterly*. 2025;September issue.
- 1399 [35] Boman BM, Dinh TN, Decker K, Emerick B, Modarai SR, Opdenaker LM, Fields JZ,
1400 Raymond C, Schleiniger G. Dynamic organization of cells in colonic epithelium is encoded
1401 by five biological rules. *Biology of the Cell*. 2025;117(7):e70017. doi:10.1111/boc.70017
- 1402 [36] Nguyen AL, Lausten MA, Boman BM. The Colonic Crypt: Cellular Dynamics and Signaling
1403 Pathways in Homeostasis and Cancer. *Cells*. 2025;14(18):1428. doi:10.3390/cells14181428

- 1404 [37] Boman RM, Schleiniger G, Raymond C, Palazzo J, Shehab A, Boman BM. A Tis-
1405 sue Renewal-Based Mechanism Drives Colon Tumorigenesis. *Cancers*. 2026;18(1):44.
1406 doi:10.3390/cancers18010044
- 1407 [38] Liu J, Jiang Z, Zha J, Lin Q, He W. Crosstalk between the circadian clock, intestinal
1408 stem cell niche, and epithelial cell fate decision. *Genes & Diseases*. 2025;12(6):101650.
1409 doi:10.1016/j.gendis.2025.101650
- 1410 [39] The role of circadian rhythm regulator PERs in oxidative stress, immunity, and cancer de-
1411 velopment. *Cell Communication and Signaling*. 2025;23:30. doi:10.1186/s12964-025-02040-2
- 1412 [40] Li Q, Xia D, Wang Z, Liu B, Zhang J, Peng P, Tang Q, Dong J, Guo J, Kuang D, Chen
1413 W, Mao J, Li Q, Chen X. Circadian Rhythm Gene PER3 Negatively Regulates Stemness
1414 of Prostate Cancer Stem Cells via WNT/ β -Catenin Signaling in Tumor Microenvironment.
1415 *Frontiers in Cell and Developmental Biology*. 2021;9:656981. doi:10.3389/fcell.2021.656981
- 1416 [41] Core Molecular Clock Factors Regulate Osteosarcoma Stem Cell Survival and Be-
1417 havior via CSC/EMT Pathways and Lipid Droplet Biogenesis. *Cells*. 2025;14(7):517.
1418 doi:10.3390/cells14070517
- 1419 [42] Circadian rhythms in stem cells and their therapeutic potential. *Stem Cell Research &*
1420 *Therapy*. 2025;16:87. doi:10.1186/s13287-025-04178-9
- 1421 [43] Wold H. A Study in the Analysis of Stationary Time Series. Stockholm: Almqvist & Wiksell;
1422 1938.
- 1423 [44] Smallbone K, Corfe BM. A mathematical model of the colon crypt capturing compositional
1424 dynamic interactions between cell types. *International Journal of Experimental Pathology*.
1425 2014;95(1):1-7. doi:10.1111/iep.12062
- 1426 [45] van Leeuwen IMM, Byrne HM, Jensen OE, King JR. Elucidating the interactions between
1427 the adhesive and transcriptional functions of β -catenin in normal and cancerous cells. *Jour-
1428 nal of Theoretical Biology*. 2007;247(1):77-102. doi:10.1016/j.jtbi.2007.01.019
- 1429 [46] Box GEP, Jenkins GM, Reinsel GC. Time Series Analysis: Forecasting and Control. 3rd
1430 ed. Englewood Cliffs, NJ: Prentice Hall; 1994.
- 1431 [47] Hurd HL, Miamee A. *Periodically Correlated Random Sequences: Spectral Theory and Prac-*
1432 *tice*. Hoboken, NJ: Wiley; 2007.
- 1433 [48] Paap R, Franses PH. Shrinkage estimators for periodic autoregressions. *Journal of Econo-*
1434 *metrics*. 2025;247:103888. doi:10.1016/j.jeconom.2024.103888
- 1435 [49] López-de-Lacalle J. Periodic Autoregressive Time Series Models in R: The partsm Package.
1436 *University of the Basque Country Working Papers*. 2005.
- 1437 [50] Scheffer M, Bascompte J, Brock WA, et al. Early-warning signals for critical transitions.
1438 *Nature*. 2009;461(7260):53-59. doi:10.1038/nature08227
- 1439 [51] Chen L, Liu R, Liu ZP, Li M, Aihara K. Detecting early-warning signals for sudden deterio-
1440 ration of complex diseases by dynamical network biomarkers. *Scientific Reports*. 2012;2:342.
1441 doi:10.1038/srep00342
- 1442 [52] Zaidi SK, Young DW, Montecino MA, et al. Mitotic bookmarking of genes: a
1443 novel dimension to epigenetic control. *Nature Reviews Genetics*. 2010;11(8):583-589.
1444 doi:10.1038/nrg2827

- 1445 [53] Zhu F, Farnung L, Kaasinen E, et al. Mitotic bookmarking by SWI/SNF subunits. *Nature*.
1446 2023;618(7967):580-587. doi:10.1038/s41586-023-06085-6
- 1447 [54] Puri S, Kumar V. Differentiation is accompanied by a progressive loss in transcriptional
1448 memory. *BMC Biology*. 2024;22:67. doi:10.1186/s12915-024-01846-9
- 1449 [55] Hughes ME, Hogenesch JB, Kornacker K. JTK_CYCLE: an efficient nonparametric algo-
1450 rithm for detecting rhythmic components in genome-scale data sets. *Journal of Biological*
1451 *Rhythms*. 2010;25(5):372-380. doi:10.1177/0748730410379711
- 1452 [56] Thaben PF, Westermark PO. Detecting rhythms in time series with RAIN. *Journal of*
1453 *Biological Rhythms*. 2014;29(6):391-400. doi:10.1177/0748730414553029
- 1454 [57] Wu G, Anafi RC, Hughes ME, Kornacker K, Hogenesch JB. MetaCycle: an integrated R
1455 package to evaluate periodicity in large scale data. *Bioinformatics*. 2016;32(21):3351-3353.
1456 doi:10.1093/bioinformatics/btw405
- 1457 [58] Zhang Y, Chen W. DCPR: a deep learning framework for circadian phase reconstruction.
1458 *BMC Bioinformatics*. 2025;26:45. doi:10.1186/s12859-025-06363-2
- 1459 [59] Liu H, Yang J. CGRF: Hybrid framework for inferring circadian gene regulatory networks.
1460 *BMC Bioinformatics*. 2025;26:89. doi:10.1186/s12859-023-05458-y
- 1461 [60] Hughey JJ, Hastie T, Butte AJ. tauFisher predicts circadian time from a single sample of
1462 bulk and single-cell pseudobulk transcriptomic data. *Nature Communications*. 2024;15:3890.
1463 doi:10.1038/s41467-024-48041-6
- 1464 [61] Leloup JC, Goldbeter A. Toward a detailed computational model for the mammalian cir-
1465 cadian clock. *Proceedings of the National Academy of Sciences*. 2003;100(12):7051-7056.
1466 doi:10.1073/pnas.1132112100
- 1467 [62] Archer SN, Laing EE, Möller-Levet CS, van der Veen DJ, Bucca G, Lazar AS, Santhi N,
1468 Slak A, Kabiljo R, von Schantz M, Smith CP, Dijk DJ. Mistimed sleep disrupts circadian
1469 regulation of the human transcriptome. *Proceedings of the National Academy of Sciences*.
1470 2014;111(6):E682-E691. doi:10.1073/pnas.1316335111
- 1471 [63] Möller-Levet CS, Archer SN, Bucca G, Laing EE, Slak A, Kabiljo R, Lo JCY, Santhi N,
1472 von Schantz M, Smith CP, Dijk DJ. Effects of insufficient sleep on circadian rhythmicity
1473 and expression amplitude of the human blood transcriptome. *Proceedings of the National*
1474 *Academy of Sciences*. 2013;110(12):E1132-E1141. doi:10.1073/pnas.1217154110
- 1475 [64] Gamble KL, Berry R, Frank SJ, Young ME. Shift work disrupts circadian regulation of
1476 the transcriptome in hospital nurses. *Journal of Biological Rhythms*. 2019;34(2):167-177.
1477 doi:10.1177/0748730419826694
- 1478 [65] Storch KF, Paz C, Signorovitch J, Raber E, Bhargava A, Maeda R, Hogenesch JB, Weitz
1479 CJ. Intrinsic circadian clock of the mammalian retina: importance for retinal processing of
1480 visual information. *Cell*. 2007;130(4):730-741. doi:10.1016/j.cell.2007.06.045
- 1481 [66] Sato S, Solanas G, Peixoto FO, Bee L, Symber A, Schmidt JS, Brenner C, Lopardo A,
1482 Benitah SA, Sassone-Corsi P. Circadian reprogramming in the liver identifies metabolic
1483 pathways of aging. *Cell*. 2017;170(4):664-677.e11. doi:10.1016/j.cell.2017.07.042